3D structural implicit modelling of folded metamorphic units at Lago di Cignana with uncertainty assessment

Gloria Arienti, Andrea Bistacchi, Guillaume Caumon, Bruno Monopoli, Giovanni Dal Piaz

Journal of Structural Geology 191 (2025) 105329

Contents lists available at ScienceDirect

Journal of Structural Geology

journal homepage: www.elsevier.com/locate/jsg

3D structural implicit modelling of folded metamorphic units at Lago di Cignana with uncertainty assessment

Gloria Arienti [a,*], Andrea Bistacchi [a], Guillaume Caumon [b,c], Bruno Monopoli [d], Giovanni Dal Piaz [d]

[a] Dipartimento di Scienze dell'Ambiente e della Terra, Università degli Studi di Milano-Bicocca, 20126, Italy
[b] GeoRessources – ENSG, Université de Lorraine - CNRS, 54000, France
[c] Institut Universitaire de France (IUF), 75000, France
[d] LTS s.r.l., Treviso, 31020, Italy

ARTICLE INFO

Keywords:
3D implicit modelling
Uncertainty analysis
Metamorphic mountain belt
Pennine Alps
Alpine tectonic contacts
Isoclinal recumbent folds

ABSTRACT

We present a modelling workflow for the creation of a km-scale, three-dimensional representation of the tectonic architecture exposed in the Lago di Cignana region within the Italian Pennine Alps. The model portrays notable tectonic boundaries such as the Dent Blanche Basal Thrust, the Combin Fault and the Roisan-Cignana Shear Zone. Our approach employs the implicit Discrete Smooth Interpolator, which represents the tectonic sequence as a volumetric scalar field generalising a relative distance function. The interpolation process is constrained by geological and structural field data. To model folds that outcrop in the region, we perform three-dimensional interpolation of fold axes, and we enforce these interpolated directions on the fold geometries through tangent constraints complementing the regularisation term in the least-squares system. Furthermore, we address structural uncertainty on isoclinal recumbent folds exposed in the area by simulating a collection of virtual data at randomly located outcrops and stochastically simulating fold axes away from direct observations. These simulated fold axes are arranged in spherical orientation distributions consistent with field data and are used as additional constraints for implicit interpolation. The uncertainty analysis generates multiple scenarios for non-cylindrical folds in terms of axis orientations and interlimb angle.

1. Introduction

Three-dimensional structural models are numerical representations of geological units in the subsurface. They are built by interpolating between sample data while adhering to the logical rules and procedures of geological reasoning (*sensu* Frodeman, 1995; Wellmann and Caumon, 2018) to accurately represent the geometry and topology of the subsurface (Mallet, 2002). When depicting metamorphic terrains, their creation is a challenging task that requires understanding of both the ductile and brittle deformation and metamorphic processes responsible for the progressive development of the tectonic architecture, and the utilisation of geomodelling workflows for their representation (e.g., Maxelon and Mancktelow, 2005). Geomodelling algorithms therefore require the ability to handle structures such as isoclinal and/or recumbent folds (organised with disharmonic and multi-scale patterns), shear zones (with hierarchical relationships that define large thickness variations), and networks of faults.

In particular, the implicit geomodelling approach, which represents geological boundaries as isovalue surfaces inside a three-dimensional scalar field (Lajaunie et al., 1997), constitutes an effective method for addressing these challenges (e.g., Maxelon and Mancktelow, 2005; Bistacchi et al., 2008; Calcagno et al., 2008; Maxelon et al., 2009; Hillier et al., 2013; Vollgger et al., 2015; Philippon et al., 2015; de Kemp et al., 2016; Schneeberger et al., 2017; Thornton et al., 2018; De La Varga et al., 2019; Grose et al., 2021; Arienti et al., 2024). The approach is based on modelling principles first theorised by Houlding (1994) and Lajaunie et al. (1997), and it is also known as scalar potential field method (Chilès et al., 2004). Constrained by geological data, the method builds an analogy between a volumetric scalar field and the relative distance among geological boundaries, enabling the simultaneous integration of geological information, fault data and unconformities to build a model that is consistent with field observations.

The interpolation of implicit 3D models can be controlled by structural information (e.g., foliation measurements, fold axes, and

* Corresponding author. Piazza della Scienza, 4, 20126 Milano, Italy
E-mail address: gloria.arienti@unimib.it (G. Arienti).

https://doi.org/10.1016/j.jsg.2024.105329
Received 1 May 2024; Received in revised form 4 December 2024; Accepted 6 December 2024
Available online 15 December 2024

mineralogical lineation data), by imposing orientation constraints on the gradient of the scalar field (Frank et al., 2007; Calcagno et al., 2008; Caumon et al., 2013; Hillier et al., 2013, 2014; Laurent et al., 2016; Grose et al., 2017; Irakarama et al., 2022). This ability can be further extended to the interpolation of vectorial fields for the propagation of structural data in the three-dimensional space. Such approach has been employed for the modelling of complexly folded terrains by Hillier et al. (2013) through the interpolation of strike and dip data, and by Laurent et al. (2016) and Grose et al. (2017) through the definition and propagation of fold parameters, enhancing geological knowledge and realism.

The implicit geomodelling approach moreover offers swift adaptability to changes in the input constraining database. The efficiency in updating the interpretation when new data becomes available paves the way to the incorporation of uncertainty analysis and stochastic simulations in the geomodelling workflows (Chilès et al., 2004; Caumon et al., 2007; Wellmann et al., 2010; Lindsay et al., 2012; Wellmann and Regenauer-Lieb, 2012; Cherpeau and Caumon, 2015; Grose et al., 2018, 2019; Pakyuz-Charrier et al., 2018), strengthening the robustness of the outcomes and capturing uncertainties related to the modelling framework (i.e., structural input database, geological knowledge, and modelling algorithm). Uncertainty assessment in folded terranes has, nonetheless, received little attention. Notably, Grose et al. (2018, 2019) propose to infer fold parameters from field data in a Bayesian framework, but their fold model (Grose et al., 2017) relies on periodic assumptions which are not always met in practice as natural folds are often non-periodic and/or polyharmonic (Ramsay, 1967; Nabavi and Fossen, 2021). On the other hand, one of the goals of this paper is to investigate uncertainty assessment based primarily on axial directions using a statistical approach.

The northwestern Alps, with a complex architecture shaped by processes of metamorphic nappe emplacement (Argand, 1911; Diehl et al., 1952) and a history of more than two centuries of geological investigations (Dal Piaz, 2001), serve as an ideal natural laboratory to further explore the application of implicit geomodelling algorithms to mountain belts. In this study, we employ the implicit approach for the representation of the metamorphic units exposed in the vicinity of the Lago di Cignana (Cignana Lake, 2149 m a.s.l.), Becca di Salè (Mount Salè, 3107 m a.s.l.), and Mont Pancherot (Mount Pancherot, 2614 m a.s.l.). In particular, this study proposes to model major Alpine tectonic contacts, such as the Roisan-Cignana Shear Zone, the Dent Blanche Basal Thrust, and the Combin Fault (Ballèvre and Merle, 1993; Manzotti et al., 2014a, 2014b), by integrating structural observations obtained at the outcrop and geological map scales. These structural measurements capture various deformation events which, although not individually analysed in the present study, have progressively transposed the original fabric under non-coaxial, mainly simple shear deformation and led to strong parallelisation of the metamorphic foliations at all scales.

The Northern Aosta Valley (northwestern Italian Alps) has recently been the subject of a regional-scale 3D modelling project covering ca. 1500 km^2, extending from the Mont Blanc to the Monte Rosa (Arienti et al., 2024). In the present work, we revisit and enhance the three-dimensional modelling of the Cignana area, included in the model by Arienti et al. (2024), by significantly refining the model's resolution and detailing fold geometries that could not appear in the previous regional interpretation because of sub-scale features with regard to the regional model's resolution. In particular, we focus on isoclinal recumbent folds outcropping in the study area and present a modelling solution that relies on three-dimensional interpolation of field fold axes to successfully represent non-cylindrical folds from their map trace, without relying on structural interpretations on vertical cross-sections, with a significant improvement with respect to what we presented in Arienti et al. (2024). Lastly, we complete the modelling workflow by performing an uncertainty analysis that leverages stochastic simulation of fold axes according to field-derived spherical distributions to identify the areas of larger uncertainty within the folds.

After summarising the geological context and the tectonic history of the rock units exposed within the study area (Section 2), we introduce the geomodelling workflow used to interpolate folded structures and to perform the associated uncertainty analysis (Section 3). In Section 4, we present the modelled outcomes and discuss the results in terms of implicit modelling choices. We then discuss the results of the uncertainty analysis comparing the outcomes of different spherical distributions, specifically the von Mises-Fisher and Kent distributions.

2. Geological and tectonic setting

The northwestern Alps occupy a central position within the tectonic framework of the Alpine belt and are noteworthy for exposing the remnants of the fossil oceanic-continental suture between the European and Adriatic plates (Coward and Dietrich, 1989; Steck et al., 1999; Dal Piaz et al., 2003). This tectonic suture can be traced following the ophiolitic units of the Piedmont nappe system, which are now interleaved between the juxtaposed Austroalpine nappe system and the underlying Penninic units, respectively associated with rocks from the Adriatic and European passive margins (Dal Piaz et al., 2003). Collectively, this tectonic sequence forms the Austroalpine-Penninic collisional wedge (Dal Piaz and Ernst, 1978), marked by a blueschist-to-eclogite-facies imprint of Cretaceous-Eocene age and a Barrovian overprint (Dal Piaz et al., 2003). Within this collisional wedge, we recognise different tectono-metamorphic units as discrete crustal elements characterised by specific associations of lithology, metamorphic conditions, and tectonic evolution, stacked along tectonic boundaries that underwent a complex history of both contractional and extensional events (e.g., Reddy et al., 2003; Manzotti et al., 2014a). The succession of these tectonic events has created hierarchical relationships among the tectonic contacts exposed in the area, and progressively reworked and transposed fabrics internal to the units.

The Cignana area, which exposes rock units from both the Austroalpine and Piedmont systems, is situated within the Austroalpine-Penninic collisional wedge. The continental component is represented by the Dent Blanche-Sesia Lanzo system (Argand, 1909, 1911; Manzotti et al., 2014a), a major composite system of thrust sheets of which only the Dent Blanche system, Argand's (1906) Dent Blanche nappe *sensu lato* (DB s.l.), outcrops in our study area. This tectonic stack is in turn distinguished into two subnappes, the overlying Dent Blanche nappe *sensu stricto* (DB s.s.) and the underlying Mont Mary-Cervino superunit (MMC). These are separated by the Roisan-Cignana Shear Zone (RCSZ), a corridor of metasediments and basement rocks that experienced high localised deformation (Manzotti et al., 2014b). The spatial and structural relationships among these tectonic units are represented in Fig. 1, using the acronyms employed in this section.

Within the portion of the DB s.s. nappe exposed in our model, we identify the Arolla unit (AR), composed of Permian-age intrusive bodies that underwent Alpine blueschist to greenschist facies metamorphism (Compagnoni et al., 1977). The RCSZ, which represents the lower boundary of the DB s.s., is composed of metasediments from Mesozoic non-oceanic sequences (traditionally called Roisan zone; Diehl et al., 1952) and slivers of basement rocks from AR and MMC. According to Manzotti et al. (2014a), the tectonic amalgamation within the RCSZ occurred under blueschist facies metamorphic conditions during the Alpine subduction and exhumation cycle. This was coupled with isoclinal folding under top-to-NW shear kinematics. Subsequent greenschist facies re-equilibration took place during further nappe exhumation and large-scale folding of the units during continental collision.

Underlying the RCSZ, we find MMC, which is further distinguished into two tectono-metamorphic units that share strong similarities with the DB s.s. (Dal Piaz et al., 2016). The upper unit (MM), akin to the upper unit of the DB s.s. (which is not comprised in our study area), consists of mainly paragneisses with pre-Alpine high-grade imprint (kinzigites and migmatites). It is tectonically juxtaposed with the lower Mont Mary unit (MY), which includes gneisses and meta-pelites that experienced Alpine blueschist peak metamorphism. Both units underwent Alpine

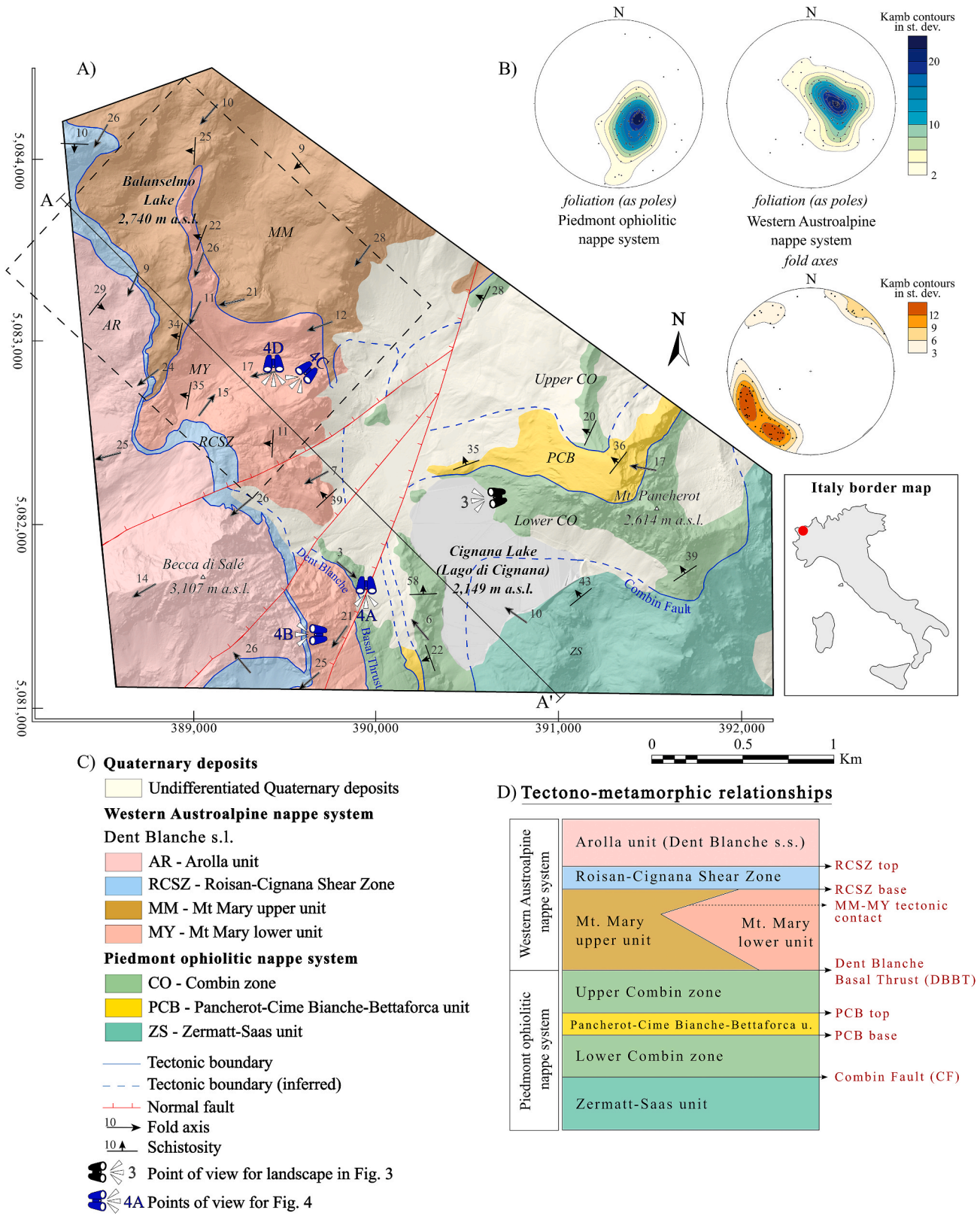

C) **Quaternary deposits**

Undifferentiated Quaternary deposits

Western Austroalpine nappe system

Dent Blanche s.l.

AR - Arolla unit

RCSZ - Roisan-Cignana Shear Zone

MM - Mt Mary upper unit

MY - Mt Mary lower unit

Piedmont ophiolitic nappe system

CO - Combin zone

PCB - Pancherot-Cime Bianche-Bettaforca unit

ZS - Zermatt-Saas unit

Tectonic boundary

Tectonic boundary (inferred)

Normal fault

Fold axis

Schistosity

3 Point of view for landscape in Fig. 3

4A Points of view for Fig. 4

D) **Tectono-metamorphic relationships**

Fig. 1. Surface input data of the Cignana Lake region. A) structural map, with only a few fold axes and schistosity measurements and coordinates as WGS 1984 UTM Zone 32N. A black dashed rectangle represents the subarea for the uncertainty analysis detailed in Sect. 3.6. B) Normal to foliation planes are plotted as dot in stereograms, with Kamb contouring interval 1 σ (Cardozo and Allmendinger, 2013; Allmendinger et al., 2015). Fold axes measured in the field are represented as dots in stereogram, with Kamb contouring interval 1.5 σ. A total of 91 schistosity measurements are represented for the Piedmont nappe, and 109 schistosity measurements and 94 fold axes are represented for the Western Austroalpine nappe system. C) Tectonic legend. D) Scheme of the tectono-metamorphic relationships.

greenschist facies metamorphism during nappe exhumation (Diehl et al., 1952; Manzotti, 2011; Dal Piaz et al., 2016).

The basal tectonic contact of the DB s.l. is marked by the Dent Blanche Basal Thrust (DBBT; e.g., Wust and Silverberg, 1989), underlain by the ophiolitic Combin zone (CO), which is part of the Piedmont nappe system, the remnant of the Mesozoic Piedmont-Ligurian ocean. The DBBT is a mylonitic boundary that records multiple reactivations, from the Eocene onwards, under decreasing greenschist facies conditions, with both reverse- and normal-sense kinematics and with no clear relationships with the oceanic subduction stage (Wust and Silverberg, 1989; Kirst, 2017).

CO displays an ophiolite-bearing succession of terrigenous and carbonatic metasediments (calcschists, *schistes lustrés*), with metabasalts, metagabbros and serpentinites (Ernst and Dal Piaz, 1978). Within our study area, CO is further subdivided into an upper and lower unit, separated by the Pancherot-Cime Bianche-Bettaforca unit (PCB), a décollement cover unit detached from an uncertain basement and showing affinities with the sedimentary succession of the Austroalpine nappe system (Dal Piaz, 1999; Passeri et al., 2018). It is interpreted as a remnant of the sedimentary cover of extensional allochtons originally distributed along the ocean-continent transition, in proximity of the Adria margin (Passeri et al., 2018). CO underwent metamorphism

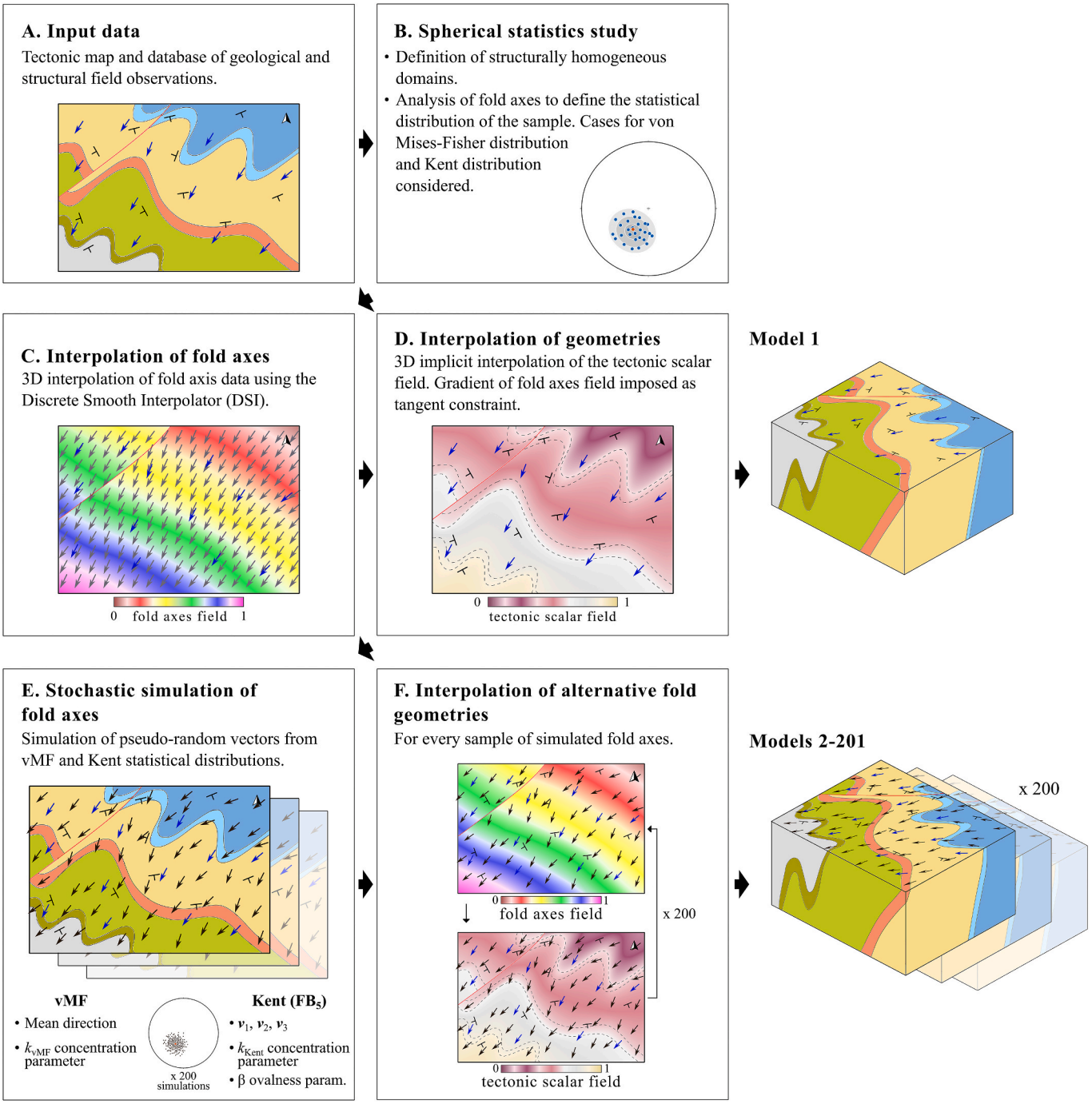

Fig. 2. Geomodelling workflow, detailed in Sect. 3. A) Input data. B) Spherical statistics analysis on the structural database. C) 3D interpolation of direct measurements of fold axes. D) Interpolation of geometries. E) Stochastic simulation of fold axes derived by von Mises-Fisher (vMF) and Kent distributions. F) Interpolation of alternative scenarios.

peaking at blueschist facies conditions (Caby, 1981; Manzotti et al., 2021), and both CO and PCB experienced metamorphism under greenschist facies conditions during post-collisional times (Ernst and Dal Piaz, 1978).

The Combin Fault (CF; Ballèvre and Merle, 1993), the second major Alpine contact exposed within the Cignana area, forms the lower boundary of CO and separates it from the underlying Zermatt-Saas unit (ZS). ZS is an ophiolitic sequence comprising serpentinites, peridotites, metagabbros and metabasalts (Dal Piaz and Ernst, 1978). This unit experienced eclogite facies metamorphism (Ernst and Dal Piaz, 1978; Bucher, 2005) and exceptionally ultra-high-pressure (UHP) metamorphic conditions registered in coesite- and microdiamond-hosting metasediments outcropping on the shore of the Cignana Lake (Reinecke, 1998; Forster et al., 2004; Groppo et al., 2009; Frezzotti et al., 2011). Given the large gap in metamorphic pressure conditions registered between CO and ZS, CF is interpreted to have accommodated exhumation of UHP rocks to shallower depths (Ballèvre and Merle, 1993; Reddy et al., 2003; Pleuger et al., 2007). This strain zone registers

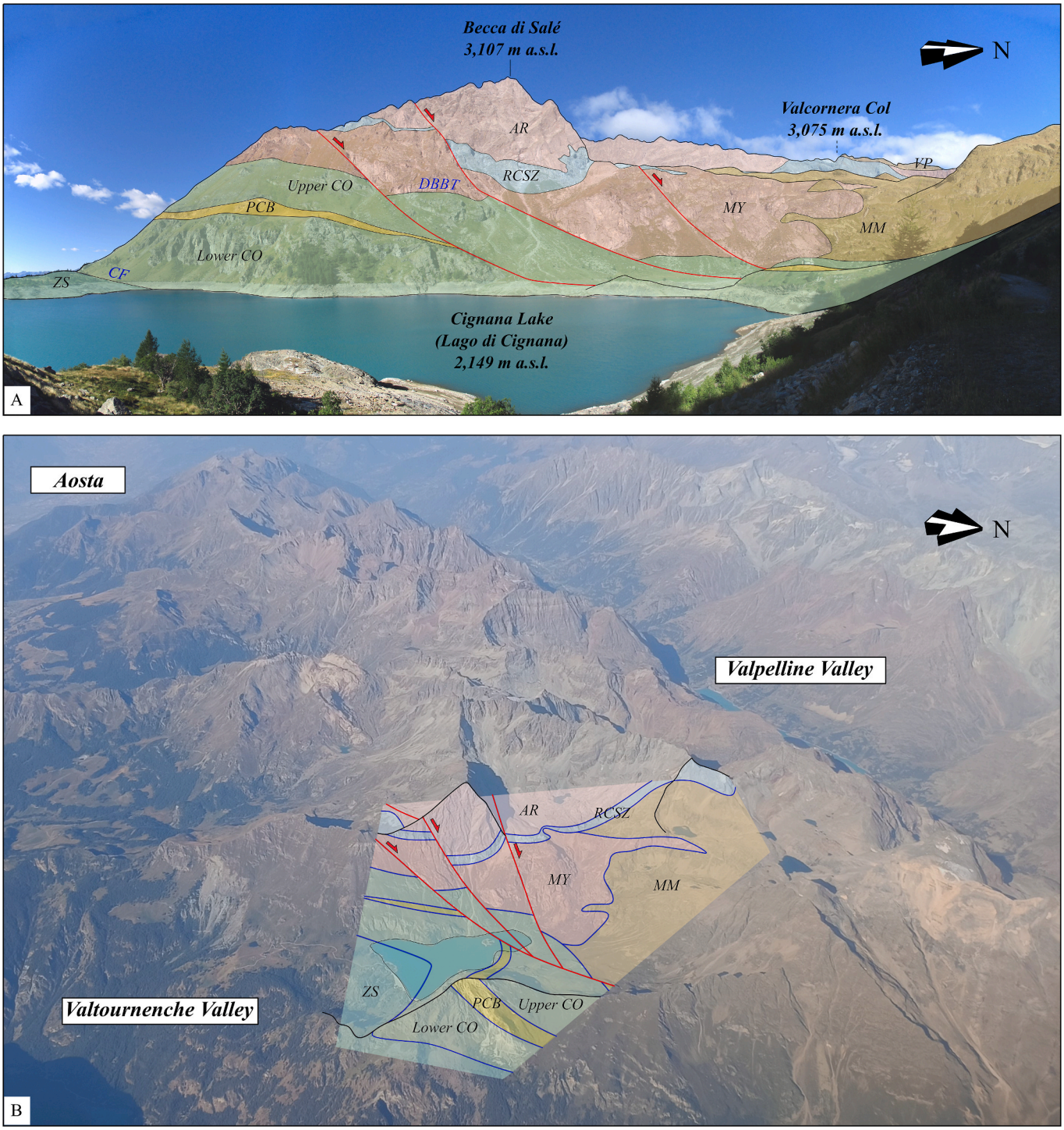

Fig. 3. Interpreted landscape views of the Cignana Lake area. Colours and names of tectonic units as in the structural map in Fig. 1, except for VP (Valpelline unit), not considered in this study. A) Terrestrial landscape view. Point of view indicated by binoculars icon in Fig. 1A. B) View from commercial plane. (For interpretation of the references to colour in this figure legend, the reader is referred to the Web version of this article.)

kinematics of both top-SE and top-NW shearing, attesting a history of reactivation and tectonic reworking since the Eocene (Reddy et al., 2003; Pleuger et al., 2007; Kirst and Leiss, 2017).

The study area has also undergone post-metamorphic extensional brittle faulting since the Oligocene. This is registered in offsets of the tectonic contacts along two NE-SW and NW-SE striking sets of brittle normal faults (Bistacchi and Massironi, 2000; Bistacchi et al., 2001; Sue et al., 2007).

3. Methodology: from field mapping to 3D structural modelling with uncertainty assessment

Our geomodelling workflow (Fig. 2) is designed to build 3D structural models conditioned by surface geological and structural data collected in the field, employing the implicit Discrete Smooth Interpolator as implemented in the RING Toolkit plugin (Frank et al., 2007; Caumon et al., 2013) running on SKUA/GOCAD (https://www.aspentech.com/en/products/sse/aspen-skua). In the following we provide details on each step of the workflow.

3.1. Input data

Our input data are summarised in the 1:75,000 new structural map of the northern Aosta Valley, which is the result of the recent upscaling of 1:10,000 original surveys published on the Geoportale Regione Autonoma Valle d'Aosta (https://geoportale.regione.vda.it/; Dal Piaz et al., 2010, 2016; Perello et al., 2011; Polino et al., 2015). A high-resolution version of the structural map, based on the 1:10,000 surveys, is shown in Fig. 1A. In addition to legacy geological and structural data derived from the map of the northern Aosta Valley, we compiled a new, field-collected dataset of metamorphic schistosity and fold axis measurements. Together, these datasets form the structural database used in this modelling work (Fig. 1B). The scheme of tectono-metamorphic relationships in Fig. 1D assigns unique names to the tectonic contacts and

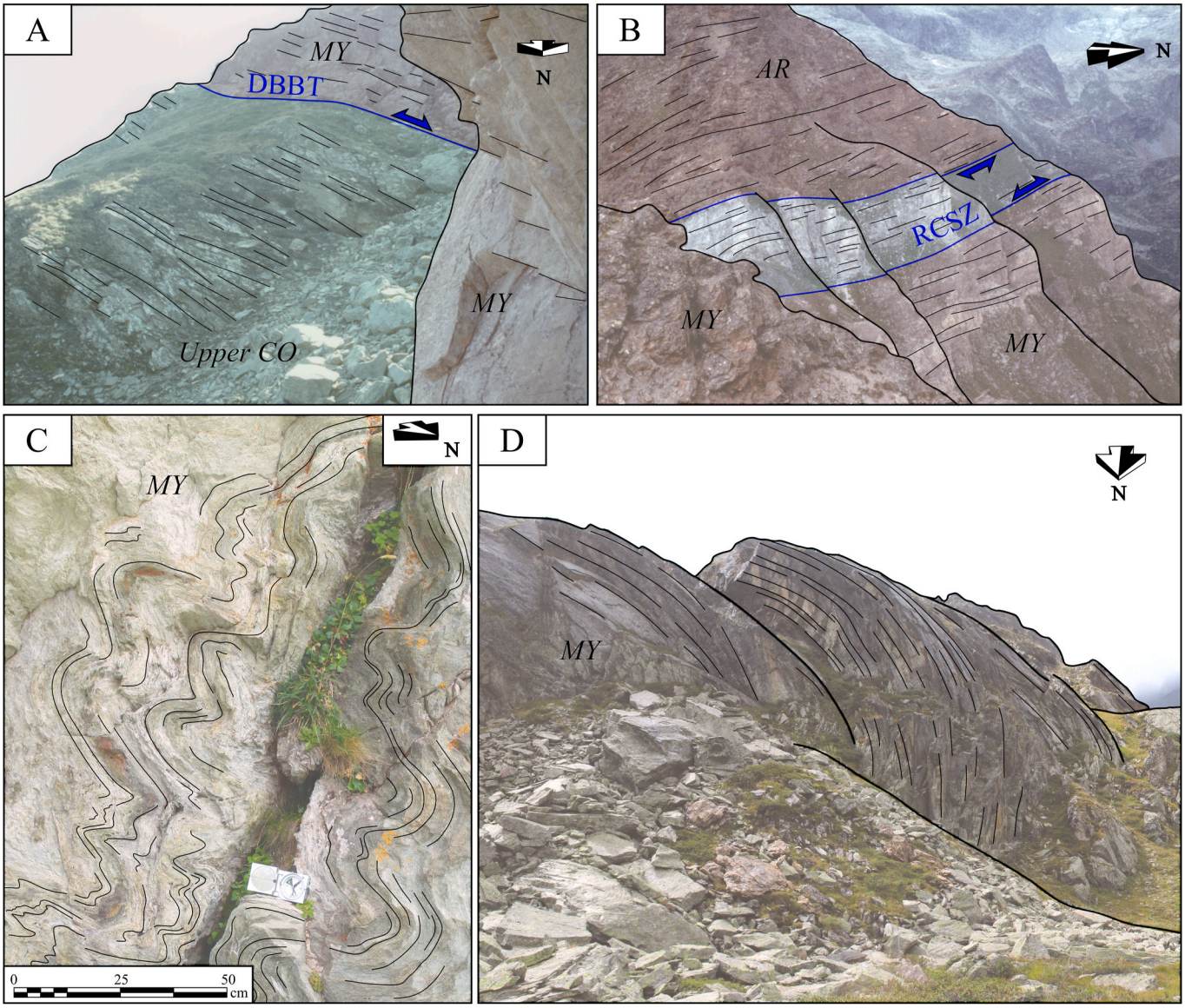

Fig. 4. Interpreted outcrop-scale views. Colours and names of the tectonic units, and location of the points of view for the photos as in the structural map in Fig. 1A. Black thin lines highlight metamorphic schistosity. A) Austroalpine unit (MY) and Piedmont unit (Upper CO) separated by the Dent Blanche Basal Thrust (DBBT). B) The Roisan-Cignana Shear Zone (RCSZ) separates AR from MY, in the Austroalpine domain. C) Outcrop-scale parasitic folds. D) Meso-scale folding of the metamorphic schistosity. Fold axes in (C) and (D) plunge at a low angle towards the WSW. Scale bars were omitted in (A), (B), and (D) as they represent different outcrops at varying distances from the camera, with the scale ranging from a few metres in the foreground to tens of metres in the background. (For interpretation of the references to colour in this figure legend, the reader is referred to the Web version of this article.)

boundaries and illustrates their hierarchical relationships. This scheme is crucial in facilitating the transfer of information between the 2D structural map and the 3D model.

Field data are organised in a GIS (Geographic Information System) and complemented by a high resolution 2 m/pixel DEM (Digital Elevation Model), obtained from a LIDAR survey, and 20 cm/pixel aerial orthophotos (provided by the Autonomous Aosta Valley region). The rugged topography of our study area results in a truly three-dimensional geological dataset, spanning over 1300 m in elevation from the highest peak (Becca di Salè, 3107 m a.s.l.) to the Cignana Valley, covering an area of ca. 9 km^2. Fig. 3 displays landscape views of the study area with interpreted tectonic boundaries and units. Fig. 4 presents outcrop-scale views of selected portions of the study area (as located in Fig. 1), showing the parallelisation between metamorphic foliation and tectonic contacts (Fig. 4A and B) as a result of the Alpine transposition of older fabrics, and outcrop and meso-scale folds (Fig. 4C and D).

3.2. Structural data analysis

The structural analysis step of our workflow is aimed at (i) identifying subareas governed by homogeneous structural behaviour (e.g., showing consistent foliation data or folding styles) and (ii) defining the spherical statistics distributions for the stochastic simulation of fold axes data. Results are in Sect. 4.

The structural analysis is performed on the three-component unit vectors (*easting*, *northing*, *elevation*) of the structural linear measurements, computed using the standard transformation from spherical to Cartesian coordinates:

$$easting = L_i = cos(plunge)sin(trend), \tag{1}$$

$$northing = M_i = cos(plunge)cos(trend), \tag{2}$$

$$elevation = N_i = -sin(plunge). \tag{3}$$

Firstly, we identify subareas displaying homogeneous structural behaviour, such as consistent foliation attitude or folding styles (e.g., Bistacchi et al., 2008). This also implies detecting boundaries that mark abrupt shifts in deformation styles, which often correspond to tectonic contacts separating different domains.

We then proceed to analyse the statistical distribution of the database of fold axes falling within the area in which the uncertainty analysis will be performed (methodology in Sect. 3.6). First, we perform a preliminary exploratory step to examine the orientation, clustering and shape of the data sample (composed of n measurements) through eigen analysis. Consider the orientation tensor A formed by the average outer product of the orientation data (Woodcock, 1977):

$$A = \frac{1}{n}\begin{bmatrix} \sum_{i=1}^{n} L_i^2 & \sum_{i=1}^{n} L_i M_i & \sum_{i=1}^{n} L_i N_i \\ \sum_{i=1}^{n} M_i L_i & \sum_{i=1}^{n} M_i^2 & \sum_{i=1}^{n} M_i N_i \\ \sum_{i=1}^{n} N_i L_i & \sum_{i=1}^{n} N_i M_i & \sum_{i=1}^{n} N_i^2 \end{bmatrix}. \tag{4}$$

The three eigenvectors $(\boldsymbol{v}_1, \boldsymbol{v}_2, \boldsymbol{v}_3)$ of A describe the orthogonal principal axes of the area, with $\boldsymbol{v}_1$ being the major axis (and often an estimate of the mean direction), $\boldsymbol{v}_2$ the intermediate and $\boldsymbol{v}_3$ the minor axis. The corresponding eigenvalues (S_1, S_2, S_3) of A are directly related to fabric shape, which can be quantified computing the shape parameter K (Woodcock, 1977) as:

$$K = \frac{\ln(S_1/S_2)}{\ln(S_2/S_3)}. \tag{5}$$

Large values of K correspond to linear (prolate) orientation features whereas small values correspond to planar (oblate) features. The eigenvalues additionally allow to quantify the strength of the main orientation by computing the parameter C (Woodcock, 1977):

$$C = ln\left(S_1/S_3\right). \tag{6}$$

After eigen analysis, we proceed by characterising the statistical distribution of the data sample by computation of parameters such as mean direction and concentration of the sample. Here we present the cases for von Mises-Fisher (vMF; Fisher, 1953) and Kent (1982) distributions in order to perform simulations of both distributions in the uncertainty analysis step of our work, as we will see in Sect. 4.2. The vMF distribution on the sphere is the analogue of the isotropic bivariate normal distribution, characterised by circular contours, while the Kent distribution (also called Fisher-Bingham, or FB_5) is the analogue for the general bivariate normal distribution and it draws oval contours on the unit sphere (Kent, 1982). Both distributions describe sample datasets distributed around one axis, with the vMF assuming isotropic spread around the major axis, while the Kent distribution accommodates anisotropic spread, making it suitable for more complex patterns of directional data.

The vMF distribution is parameterised using the mean direction and concentration parameter k_{Fisher} of the sample. For n measurements, the mean direction is estimated by defining the orientation $(\overline{x}, \overline{y}, \overline{z})$ of the resultant vector R (Borradaile, 2003):

$$R^2 = \left(\sum_{i=1}^{n} L_i\right)^2 + \left(\sum_{i=1}^{n} M_i\right)^2 + \left(\sum_{i=1}^{n} N_i\right)^2, \tag{7}$$

$$\overline{x} = \frac{1}{R}\sum_{i=1}^{n} L_i,\ \overline{y} = \frac{1}{R}\sum_{i=1}^{n} M_i,\ \overline{z} = \frac{1}{R}\sum_{i=1}^{n} N_i. \tag{8}$$

The concentration parameter k_{Fisher}, which quantifies the degree of clustering of the sample around the mean direction, can be estimated by (Fisher, 1953):

$$\begin{cases} k_{Fisher} = \dfrac{n}{n-R}\left(1-\dfrac{1}{n}\right)^2 & when\ n < 16 \\ k_{Fisher} = \dfrac{n-1}{n-R} & when\ n \geq 16. \end{cases} \tag{9}$$

On the other hand, the Kent distribution is described by a concentration parameter k_{Kent}, an ovalness parameter β and the orientation matrix. The parameterisation of this distribution, which relies on the computation of maximum likelihood estimates, is not as straightforward as for the vMF case, however libraries that deal with this problem have been recently published (e.g., Yuan, 2021). The Kent distribution requires $k_{Kent} > 2\beta$ to represent a general bivariate normal distribution, while in case $\beta = 0$ it reduces to the vMF distribution (Kent, 1982).

3.3. The Discrete Smooth Interpolator: an overview

Following data analysis and preparation, we perform interpolation in 3D using the implicit Discrete Smooth Interpolator (Frank et al., 2007; Caumon et al., 2013). First implemented to represent sedimentary sequences, implicit methods model the stratigraphic sequence as a continuous, derivable scalar field (except at faults and unconformities) which represents the relative age of rock units throughout the model volume (Houlding, 1994; Lajaunie et al., 1997). Stratigraphic boundaries such as the top of formations are extracted a posteriori as isovalue surfaces of the scalar stratigraphic field and can be used to obtain a boundary representation. In our workflow, since we consider tectonic units and not stratigraphic settings, the scalar field does not correspond to the relative geological time but to the vertical axis in the tectono-metamorphic diagram (Fig. 1D).

In the workflow presented in this work we employ the DSI of SKUA/GOCAD as implemented in the RING Toolkit plugin (Frank et al., 2007; Caumon et al., 2013), which computes the scalar field values at the nodes of a tetrahedral mesh from the structural data with a weighted

least-squares approach.

Different types of constraints, each with customisable weights, control the interpolation process. Firstly, position constraints are defined based on geological information (i.e., mapped boundaries or interpretations on vertical cross-sections) that constrain the value of the scalar field at specific locations. Other constraints can be imposed that influence the gradient of the scalar field, which by definition is orthogonal to the isovalue surfaces, in different ways. Foliation attitude data can be used to align the gradient with the normal direction to the dip-dip direction plane, while the stacking direction of the succession holds the polarity information of the constraining vector. Moreover, vectors such as fold axes or lineations can be imposed as tangent constraints to bind isovalue surfaces of the implicit scalar field to the tangent vector (Caumon et al., 2013). This enforces a gradient that is maintained perpendicular to the tangent vector and, as we will see in the next section, is particularly useful for modelling complex structures such as isoclinal recumbent folds.

The gradual transition of the scalar field between two points is ensured by a continuity (smoothness) constraint imposed at faces of the tetrahedra (Frank et al., 2007). This constraint guarantees the well-posedness of the mathematical interpolation problem and is responsible for the creation of continuous and derivable scalar fields. The continuity is interrupted only at the intersection with fault surfaces and unconformities, which are therefore represented as mathematical – in addition to geological – discontinuities. This approach allows modelling both infinitely extended and finite faults (i.e., faults with tip line falling within the modelling domain).

However, hierarchical relationships such as stratigraphic or tectonic discontinuities are not handled by the RING Toolkit interpolator (Frank et al., 2007; Caumon et al., 2013) used in the present study. We solve this issue by applying mesh cutting tools, as implemented in SKUA/-GOCAD, to the boundary representation surfaces extracted from the implicit scalar field.

3.4. Interpolation of the fold axes field

Fold axes measurements collected in the field are relatively sparse and heterogeneously distributed. These are axes of outcrop-scale parasitic folds (with respect to folded major tectonic contacts, Fig. 4), and before using them as constraints to interpolate larger-scale model of major tectono-metamorphic units, their meaning must be assessed in terms of tectonic phases and cylindricity of large-scale folds (at least within subdomains of the study area), which is a fundamental precondition for the upscaling of the fold geometries (Ramsay, 1967). We will discuss these topics in the results and we will show that we are able, with some caution, to adopt a fold axes interpolation strategy inspired by the works of Philippon et al. (2015) and Laurent et al. (2016).

Fold axes represented as unit vectors (equations (1)–(3) are used in the interpolation with DSI of a three-dimensional scalar field, that we here refer to as "fold axes field" (F_{fa}; Fig. 2C). Within this field, fold axes are parallel to the gradient, and the scalar value itself represents just a dummy variable that increases along the fold axes direction. The advantage of this approach is that it honours direct measurements of fold axes (in a least-squares sense) while performing a smoothing (Frank et al., 2007; Caumon et al., 2013). This first interpolation relies on the assumption that the vector field representing the fold axes is relatively smooth. The gradient of F_{fa} (i.e., upscaled fold axes) is then enforced as tangent constraint for the interpolation of the "tectonic scalar field" (F_t; Fig. 2D) that describes the tectono-metamorphic units and their boundaries, and whose values represent the relative distance among tectonic contacts.

The use of tangent data in the weighted least-squares interpolation is a way to account for the anisotropy of folds. Indeed, the constant gradient constraint alone tends to generate unrealistic isotropic stratigraphic geometries, whereas the addition of smooth fold axes as tangent constraints locally imposes the direction of minimal curvature. Overall, the relative weights of these two terms control the degree of anisotropy of the solution.

We will show that this strategy allows accurately modelling isoclinal recumbent folds (Sect. 4.1) and paves the way for stochastic modelling of the associated uncertainty (Sect. 3.6 and applications in Sect. 4.2).

3.5. Using fold axes field to densify mapped boundaries constraints

Whereas the fold axes field controls the direction of minimal curvature of the solution, its maximum curvature only stems from the neighbouring tectonic boundary data and tends to be under-estimated away from the data because of the constant gradient term. Therefore, we exploit the geometric properties of the fold axes field F_{fa} to densify the constraints represented by the mapped tectonic boundaries. In analogy to "manual" geomodelling workflows, which often involve building a conceptual model on vertical cross-sections and using it to constrain the 3D interpolation (Kaufmann and Martin, 2009; Arienti et al., 2024), and inspired by the "plunge model" of Stockwell (1950) and de Kemp (2000), we introduce a quantitative approach to densify polylines representing mapped tectonic boundaries by multiple projections along the gradient of F_{fa} (i.e., along upscaled fold axes). This approach has advantages, with respect to manual methods, of being fast and not subject to interpretation bias (Bond, 2015).

In an iterative workflow, we project for a finite distance the mapped tectonic boundary's polylines along the direction defined by the gradient of F_{fa} at each polyline node. The local F_{fa} gradient is then transferred on nodes of the projected polyline, and the projection is repeated a number of times. The product of projection distance with the number of iterations yields the distance covered by the additional constraints. Lastly, the projected tectonic lines are used as position constraints for the interpolation of the tectonic scalar field F_t. This strategy is demonstrated in Sect. 4.1, where we apply it to model the isoclinal recumbent folds deforming the MM-MY tectonic contact. Noteworthy, since the local F_{fa} gradient is transferred at each step to be used for projecting the polylines, this approach allows for modelling folds with smoothly curved fold hinges, and not only perfectly cylindrical folds.

3.6. Stochastic simulation of fold axes for uncertainty analysis

The geomodelling workflow described above is aimed at creating deterministic models that represent the "best guess" interpretation that aligns with field data and their interpretation in terms of expert geological knowledge. In this section, we expand the workflow by introducing stochastic simulation of fold axes data that will be perturbed according to a suitable orientation distribution. We will discuss the case for both vMF (Fisher, 1953) and Kent (1982) distributions. However, the simulation approach that we present is versatile and can be easily adapted to simulate various types of vectorial data, such as dip-dip direction datasets. Additionally, this methodology can be employed to simulate other statistical distributions (Fisher et al., 1987).

Our simulation algorithm proceeds in three steps: (i) simulation of N_r samples of fold axes perturbed with a suitable orientation distribution at N_v virtual sample points; (ii) interpolation of the N_r tectonic fields using both perturbed and original axes; (iii) quantitative analysis of the results in terms of information entropy (Shannon, 1948; Wellmann and Regenauer-Lieb, 2012).

To generate pseudo-random fold axes vectors distributed according to the parameters of vMF distributions on a sphere, we employ a methodology initially introduced by Fisher et al. (1981), also applied by Wood (1994), and as presented in Appendix A in Pakyuz-Charrier et al. (2018). Given a mean vector and a concentration parameter k_{Fisher} (Fisher, 1953), the methodology creates virtual samples of unit vectors that mirror the vMF distribution. We select the mean vector and the concentration parameter k_{Fisher} based on the results of the orientation

analysis presented in Sect. 3.2, aiming to replicate the distribution observed in the input fold axes database with a larger sample size. Each simulated sample (N_r) is composed of N_v vectors, whose positions are randomly distributed within the 3D model volume, with no restrictions on the spacing between them, and whose trend/plunge values are randomly and independently sampled at each of the N_v virtual points.

To simulate pseudo-random vectors belonging to Kent distributions, we leverage the library developed by Yuan (2021) for analysis of n-parameter Fisher-Bingham distributions on the sphere. Similarly to the vMF simulations, we simulate N_r samples of N_v vectors (randomly distributed in the model volume) that follow the parameters of the Kent distribution derived from the dataset of field fold axes.

The second step of the uncertainty assessment workflow expects the implicit interpolation of fold geometries, following the approach out-

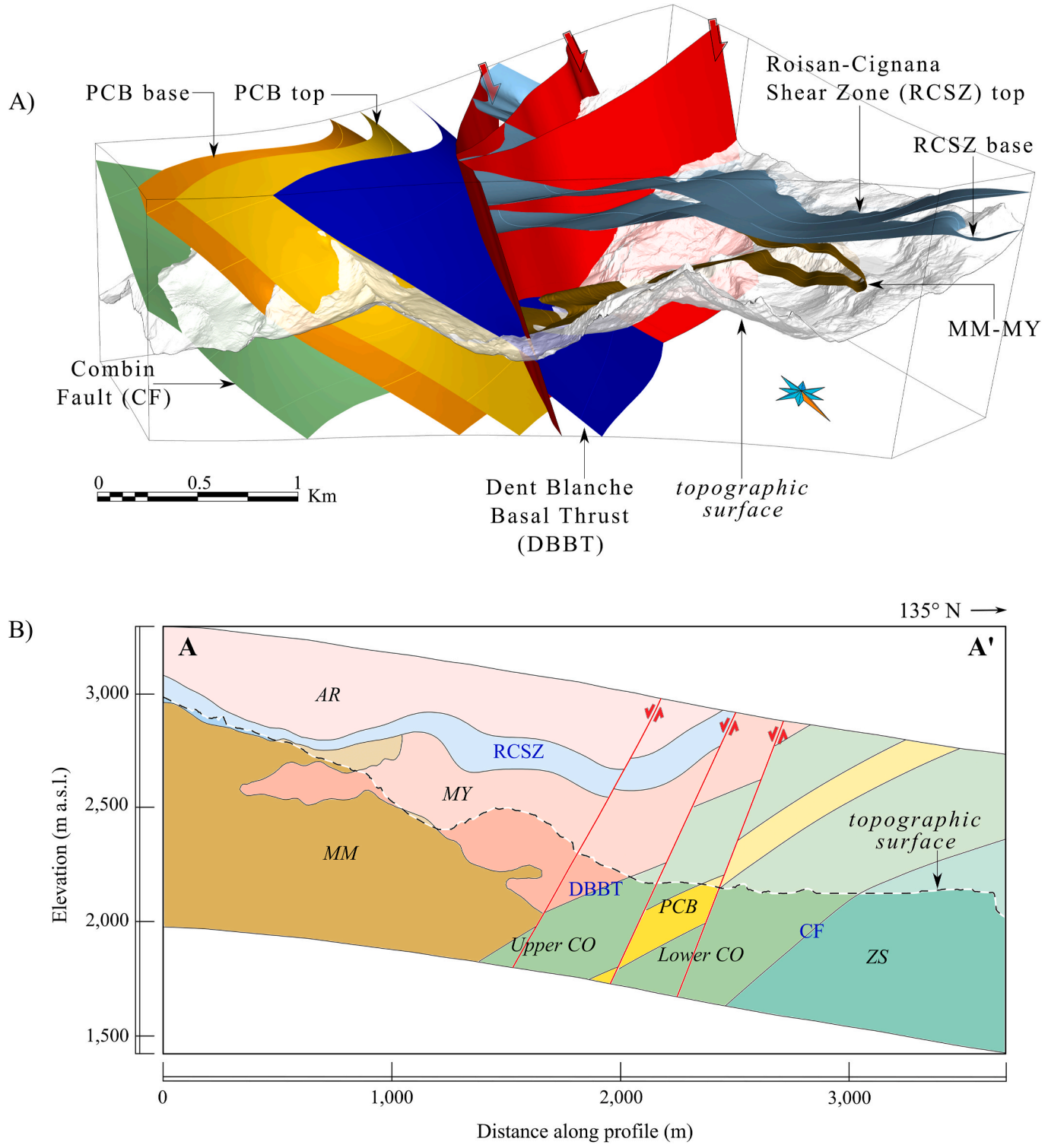

Fig. 5. 3D structural model of the Cignana Lake. Description of the model in Sect. 4.1. A) 3D view of the boundary representation with semi-transparent topographic surface. Names as in the scheme of tectono-metamorphic relationships in Fig. 1D. B) Vertical cross-section of the model. Trace of the cross-section and legend in Fig. 1.

lined in Sect. 3.4, for each set of simulated fold axes. For the interpolation of the new fold axes fields $F^{(i)}_{fa_i}, i = \{1, \ldots, N_r\}$, we consider both direct field observations and simulated virtual fold axes as constraining data, assigning higher weights (10 times higher) to the former. We proceed with the interpolation of the implicit $F^{(i)}_t$ following the general workflow (Sect. 3.4) and enforce the gradient of the newly generated $F^{(i)}_{fa}$ as tangent constraint. This results in the generation of multiple plausible tectonic contact geometries that conform to both observed and simulated data.

We measure the degree of model consistency by employing the notion of information entropy H (Shannon, 1948; Wellmann and Regenauer-Lieb, 2012), which relies on the probability p_i of every node of the tetrahedral mesh of belonging to a given tectono-metamorphic unit. Higher values of entropy in the system indicate higher uncertainty on the value of the scalar field at the node. After a number of N_r realisations have been generated, information entropy is computed at every mesh node as (Shannon, 1948; Wellmann and Regenauer-Lieb, 2012):

$$H = -\sum_{i=1}^{N_u} p_i \log p_i. \tag{10}$$

Where N_u is the total number of rock units.

4. Application to the Cignana Lake case study

In this section we present the deterministic 3D structural model of the Cignana Lake area, and we then apply the uncertainty workflow described in Sect. 3 to the isoclinal recumbent folds formed by the MM-MY tectonic contact (highlighted in Fig. 1A).

4.1. The 3D structural model of the Cignana Lake area

The 3D model has been interpolated along the nodes of a tetrahedral mesh with a roughly uniform isotropic resolution of approximately 26 m (average edge length of tetrahedra). This results in ca. 8.3×10^5 nodes and ca. 4.8×10^6 tetrahedra, which allows for practical execution times, around 10 min for interpolation of a single model, on a desktop workstation (AMD Ryzen 9 5950X Processor, NVIDIA GeForce RTX 3080 GPU, 64.0 GB RAM on a Windows system). This resolution also provides a good balance between computational efficiency and sufficient detail to model geological features accurately. The model's vertical extent covers a range of 1300 m, and the upper and lower boundaries encompass the topography. Consistently with the Alpine tradition of interpreting both subsurface and eroded spaces, the interpolated tectonic contacts extend both above and below the topographic surface to generate a continuous representation of tectonic structures and prevent edge effects. 3D and cross-section views of our structural model are shown in Fig. 5.

The 3D model also incorporates a system of three normal faults (Figs. 1 and 5), which displace tectonic contacts and that are attributed to normal faulting events that took place in brittle post-nappe conditions (Bistacchi and Massironi, 2000). Faults are integrated in the modelling workflow at an early stage, and the implicit mesh is built conformable to their surfaces. Since the faults traverse the entire model domain, they limit four independent fault blocks (Fig. 6B). According to the DSI's implementation, each of these fault blocks yields independent scalar fields and this implies that constraints whose geographical coordinates are situated between two fault surfaces solely affect the corresponding fault block and are disregarded by the others. However, the interpolation function typically requires at least two position constraints with different values and orientation data to ensure well-posedness, and this might call for virtual interpretative data points in fault blocks lacking outcrops, as we will see in the next paragraphs.

The three fault surfaces (Fig. 5) form a system consisting of a master fault and two synthetic abutting faults in the hanging-wall (Peacock et al., 2017), all dipping to the northwest at high angles ranging from 60° to 70°. According to fault kinematics data collected in the field, we have modelled them as purely dip-slip normal faults, with slip vectors sub-parallel to the branch lines (neutral relationship; Peacock et al., 2017), and with displacements ranging from 50 to 250 m.

The rock units and tectonic contacts of the Austroalpine nappe system, in the hanging-wall of the DBBT, are folded along a generally NE-SW trending system and foliation data display moderate dispersion (Fig. 1B). Several outcrop-scale, parasitic (with respect to the large-scale fold structures of the tectonic contacts) folds are exposed (Fig. 4C and D). Based on their interlimb angles, these folds draw isoclinal to open geometries. The fold axes plunge at low angles (Fig. 1A), their dispersion indicates non-cylindrical geometries, and the estimated axial surfaces dip at low, moderate, and medium angles, overall creating recumbent to reclined geometries. Their folding patterns are disharmonic and result in

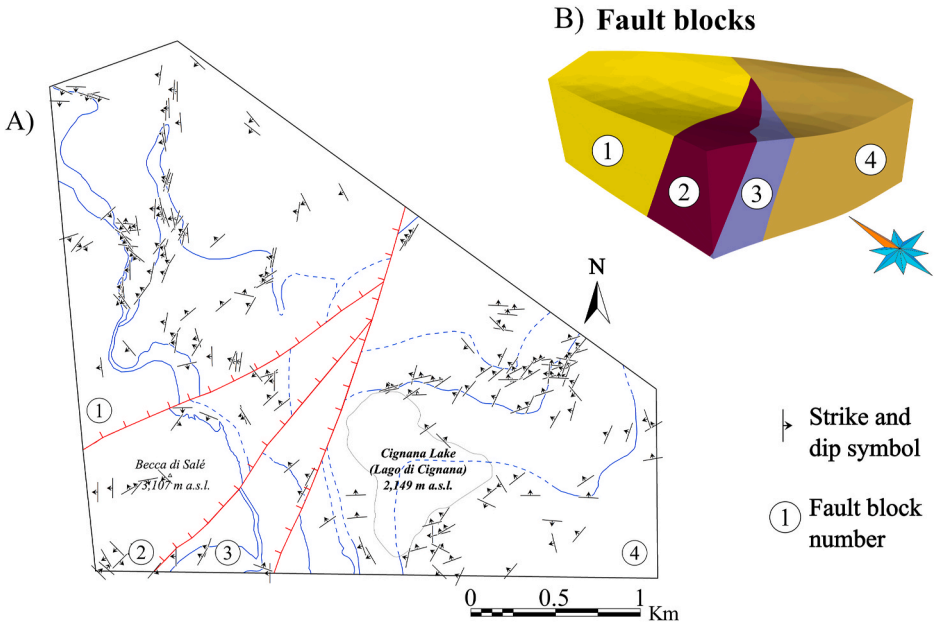

Fig. 6. Foliation data. A) Direct observations of foliation planes. B) 3D view of independent fault blocks defined by the system of synthetic normal faults.

geometries that are often challenging to trace as the scale increases beyond the outcrop scale. These geometries are also observed at a larger scale, as they fold tectonic contacts with km-scale isoclinal to open geometries (Fig. 1). The structural database for this subarea is composed of 94 direct observations of fold axes and 327 observations of schistosity planes (Fig. 6A). In contrast, in the Piedmont nappe system the structural behaviour is governed by the NW-dipping foliation, and small scale undulations within the units are attributed to the NW-SE trending parasitic folds (Fig. 1B). The structural database for these units includes 12 fold axes and 124 schistosity plane measurements.

The structural database presented above includes legacy data from the structural map of the northern Aosta Valley (https://geoportale.regione.vda.it/; Dal Piaz et al., 2010, 2016; Perello et al., 2011; Polino et al., 2015) and original measurements specifically collected for this study. The latter dataset consists of observations organised by sampling location and with large sample sizes which, for the purpose of this km-scale 3D modelling effort, are upscaled by calculating one or more representative foliation values per outcrop using mean directions (Borradaile, 2003), focusing on manually identified outcrop-scale fold limbs when present. The final structural database (Fig. 1B) used for the three-dimensional interpolation consists of 200 schistosity values (109 from the Austroalpine nappe system and 91 from the Piedmont nappe system). On the other hand, we do not upscale field fold axis data due to the fact that (1) these measurements are inherently less frequent and (2) our study focuses specifically on the interpolation of fold axes and their statistical analysis. Table 1 summarises the structural data collected in the field and the subset used for 3D modelling.

During the modelling process, we do not impose a minimum spacing between field measurements to constrain the interpolation. Instead, we rely on the regularisation term to resolve adjacent structural measurements. Moreover, as far as field conditions allow (i.e., in terms of outcrops availability and accessibility), the database of field measurements should aim to provide homogeneous coverage across the study area.

For the modelling of the RCSZ and MM-MY boundaries (Fig. 1), we employed the methodology described in Sect. 3.4, which interpolates direct fold axes measurements (Fig. 7A) into a fold axes field F_{fa} (Fig. 7B) using the RING Toolkit interpolator (Frank et al., 2007; Caumon et al., 2013). The gradient of this generated field, continuous across the model volume, is then imposed as tangent constraint on the interpolation of a second tectonic scalar field F_t that describes the geometries of the folded tectonic contacts (Fig. 7D). This approach propagates the vectorial information of the field fold axes measurements (collected at the outcrop-scale) to build a constraining field for the interpolation of the model-scale fold geometries. In addition to this, we constrained the MM-MY boundary, whose geometry is particularly complex with limbs that are locally less than 100 m apart, by applying the methodology described in Sect. 3.5 that creates additional constraining lines through projection of surface information along the F_{fa}'s gradient (Fig. 7C). Finally, we further constrain the interpolation by incorporating field foliation data as gradient constraints. Because these data are sparse and not uniformly distributed within the 3D volume – unlike the tangent constraints imposed by the interpolated fold axes – and are assigned a lower weight in the interpolation, their influence on the output geometries is consequently limited. As a result, at the scale of the 3D model, the folded geometries are largely guided by F_{fa} and the RCSZ is characterised by upright open folds, while the MM-MY boundary displays isoclinal recumbent folds.

In the southeastern portion of the model, the sequence of tectonic contacts of the oceanic Piedmont domain, together with the DBBT, forms a conformable sequence with a NW-dipping attitude affected by brittle normal faulting (Fig. 1). The interpolation of these geometries is guided by the foliation measurements (Fig. 6A) imposed as gradient constraints. However, as shown in Fig. 6, fault blocks number 1 and 2 lack outcrops of these tectono-metamorphic units, resulting in the absence of strike and dip measurements to guide the implicit interpolation. To resolve these cases, we employ geomodelling solutions informed by the structural knowledge and we assign to fault blocks number 1 and 2 an additional constraining value defined by the average foliation of the measurements collected in fault blocks number 3 and 4.

Lastly, the implicit isosurfaces generated from the scalar fields for both the Austroalpine and Piedmont systems are saved independently as triangulated meshes, creating the boundary representation of the 3D structural model (Fig. 5A).

Table 1
Summary of field measurements and structural data used for 3D modelling (Sect. 4.1).

Type of field data	Nappe system	Number of field measurements	Number of data for 3D Modelling	Notes
Foliation	Western Austroalpine	327	**109**	Foliation upscaled by calculating one or more representative values per outcrop using mean directions (Sect. 4.1)
	Piedmont	124	**91**	
Fold axes	Western Austroalpine	94	**94**	No upscaling; original field fold axes are used in 3D modeling (Sect. 4.1)
	Piedmont	12	**12**	

4.2. Simulation of fold axes for uncertainty assessment

The uncertainty analysis was carried out in the subarea of the DB s.l. system highlighted in Fig. 8A, covering an area of about 2.6 km^2. This area is of particular interest because it shows isoclinal recumbent folds of the MM-MY tectonic contact.

The subarea includes 44 measured fold axes with sub-horizontal plunge and NE-SW trend. In the equal-area plot of Fig. 8B, if analysed as a whole, the fold axes seem to show a multimodal girdle pattern that extends across the NE and SW quadrants. However, upon closer examination of the map, it becomes evident that the orientation of fold axes is not spatially uniform. Instead, we recognise two sub-areas (Sectors 1 and 2) that, if analysed separately, show distributions with a more concentrated axial symmetry. The dashed black and white line in Fig. 8A delineates the boundary between the two sectors. This line does not correspond to a particular structure or lithological boundary mapped in the field and we assume that it is related either to a refraction of strain getting closer to the MM-MY tectonic boundary or to a younger open fold.

Fold axes belonging to Sectors 1 and 2 have been independently examined through eigen analysis, following the methodology in Sect. 3.2. The results of the K and C parameters (Fig. 8B), if plotted in the two-axis plot of Woodcock (1977), show uniaxial clustering behaviour and non-isotropic axial symmetries. We proceed with the independent analysis of the two sectors, and we perform the parameterisation assuming two different scenarios. For the sake of simplicity, in the first scenario we assume that the two Sectors have been sampled from two vMF distributions (Fisher, 1953), and we therefore perform the sample parameterisation and later vector simulation following this statistics. In the second scenario, we instead assume that the two Sectors have been collected from Kent distributions (Kent, 1982) and perform the uncertainty analysis under this assumption. This choice allows us to compare the outcomes of the two scenarios and propose reasonings on how the uncertainty analysis is influenced by the assumption of isotropic or anisotropic spherical statistics.

First, we assume that the two samples are derived from vMF distributions, and we parameterise the sample with mean direction and k_{Fisher} using equations (8) and (9). We obtain mean fold axes of respectively

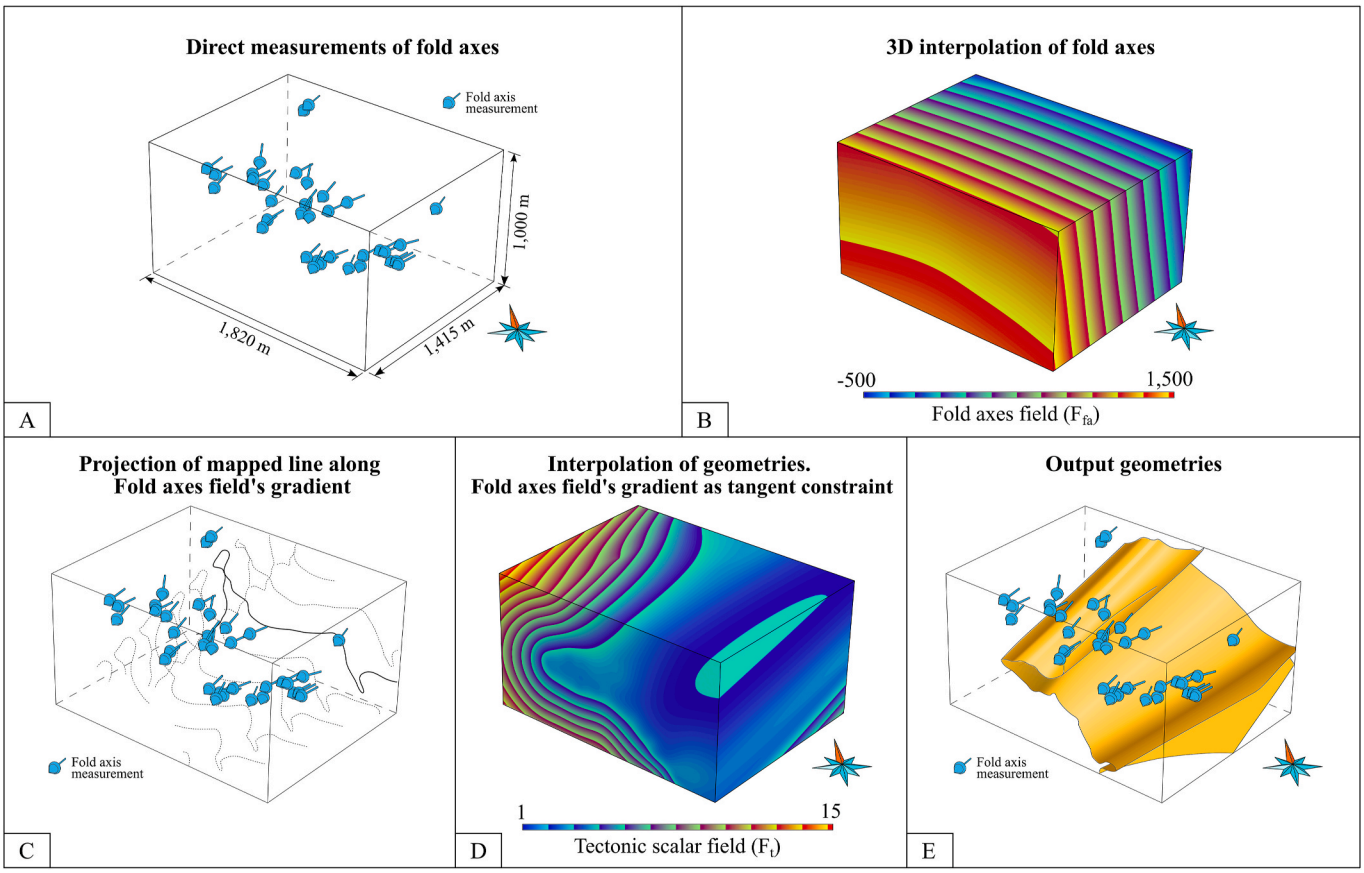

Fig. 7. Implicit interpolation steps, as detailed in Sects. 3.4 and 3.5. Location of the investigated volume is indicated in Fig. 1A by the dashed rectangle. A) Direct measurements of fold axes. B) 3D interpolation of fold axes. C) Iterative process of projection of the mapped tectonic contact along the gradient computed from (A). Only a few representative polylines are represented. D) Interpolation of geometries constrained by the gradient of the fold axes field imposed as tangent constraint. E) Output geometries.

213/08 and 251/19 (trend/plunge), and concentration parameters k_{Fisher} of values 19.0 and 110.9 (Fig. 8C). Successively, we assume Kent distributions for the two data samples and compute the spherical parameters as presented in Sect. 3.2, resulting in mean directions (corresponding to the first eigenvector) of respectively 212/08 and 251/19 (trend/plunge) for Sectors 1 and 2, concentration parameters k_{Kent} of values 20.9 and 177.8, and ovalness parameter β of 2.84 and 46.21 (Fig. 8D).

While it is evident that the two parameterisations show aligned mean directions for both samples, it can also be noticed that the assumption of Kent distribution allows detecting high ovalness for Sector 2 and only mild for Sector 1, in accordance with the computed shape parameters K, higher for Sector 1 (Fig. 8B and D). Moreover, as already suggested by the higher parameter C for Sector 2 (Fig. 8B), the Kent distributions that describe fold axes falling into Sector 2 are characterised by a high concentration parameter k_{Kent}.

To perform the interpolation of 200 geologically plausible alternative fold geometries ($N_r = 100$ under the assumption of vMF distribution, and other $N_r = 100$ for the Kent scenario), we build a three-dimensional tetrahedral mesh that covers the subarea used for the uncertainty study (Fig. 8A). The mesh has a vertical extension of 1,000 m, spanning from 2015 m a.s.l. to 3015 m a.s.l. With an isotropic resolution of 20 m (corresponding to the average distance between nodes), the mesh totals ca. 7.0×10^5 nodes and 4×10^6 cells. To maintain separation between the two homogeneous sectors in the investigated volume, the tetrahedral mesh is divided in two sub-volumes, obtained by projection of the boundary line that divides the two sectors (Fig. 8A) following the methodology of Sect. 3.5.

We generate a total of $N_r = 200$ realisations (100 per scenario), each containing $N_v = 1000$ simulated fold axes, using the spherical parameters derived from the input data. Example of stereograms of simulated fold axes, one for each distribution (vMF and Kent), are shown in Fig. 8C and D. These simulated vectors are randomly distributed throughout the 3D tetrahedral mesh, covering the whole investigated volume. Finally, we impose both original and simulated fold axes as constraints on the implicit interpolation, resulting in the computation of 100 realisations of F_{fa} and F_t (Fig. 9) per statistical distribution, following the method discussed in Sect. 3.6. The interpolation time, considering both the simulation of the new fold axes and the interpolation of the scalar field describing the folds, is in the range of 15 min per realisation.

Results of the simulations are shown in cross-sections across the simulation volume (Figs. 10 and 11), where both boundaries generated by different realisations and information entropy are displayed. In Fig. 11 we also display the difference between the information entropies obtained for the vMF and Kent scenarios ($H_{vMF} - H_{Kent}$), in order to highlight how the assumption of different spherical distributions affects the uncertainty analysis.

Larger deviations in the simulated boundaries are always observed moving away from the topographic surface, where outcrops and hence constraints are present. For instance, section D-D' (Figs. 10 and 11) exhibits well-constrained results for the isoclinal folds, as the cross-section intersects the mapped tectonic contact multiple times, providing strong constraints. Conversely, as we move farther from the topographic surface, both in the eroded and in the subsurface space, higher levels of uncertainty become evident.

We moreover notice higher uncertainties at the hinge of the isoclinal folds in sections B-B′ and C-C' (Figs. 10 and 11). Specifically, in section B-B′ the positions of the hinges exhibit a vertical oscillation of

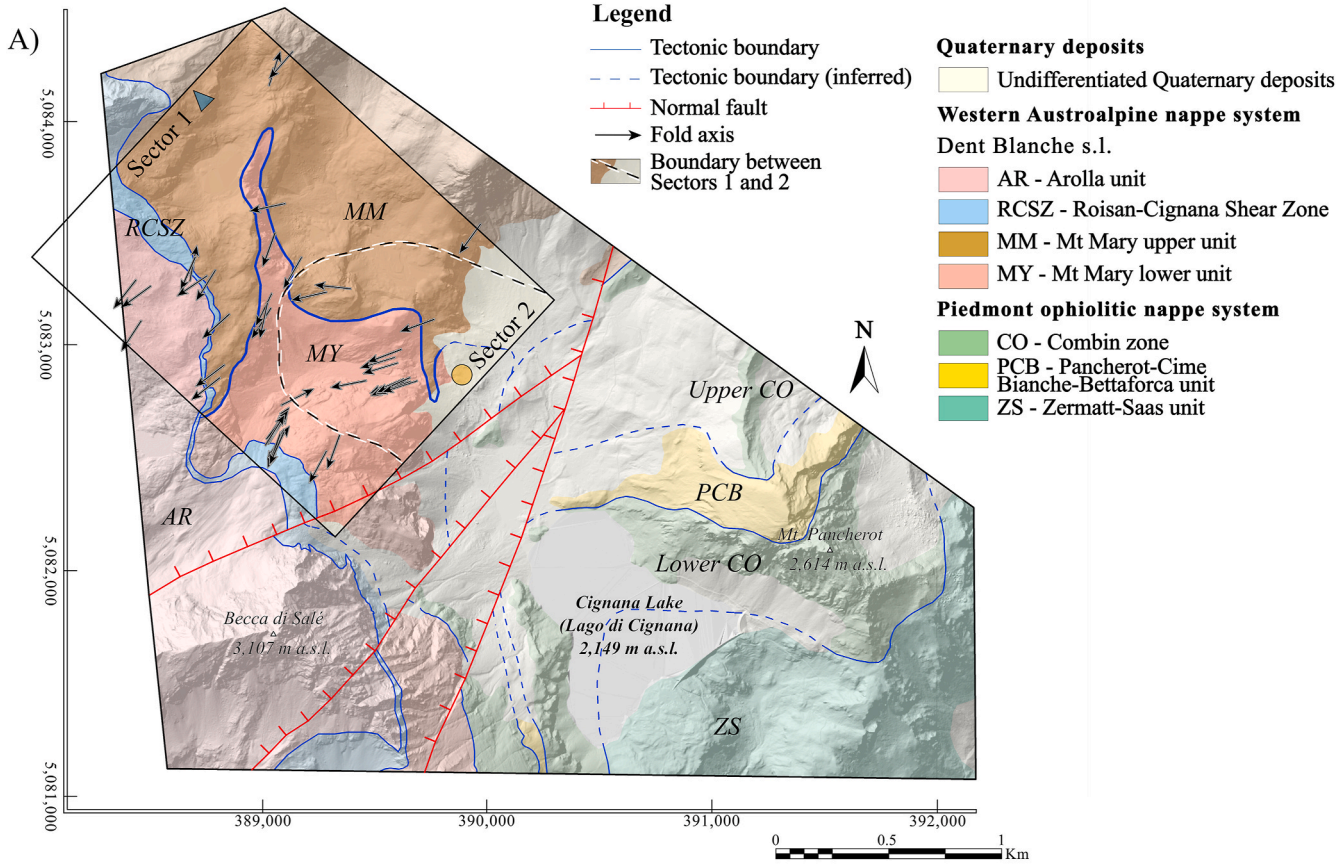

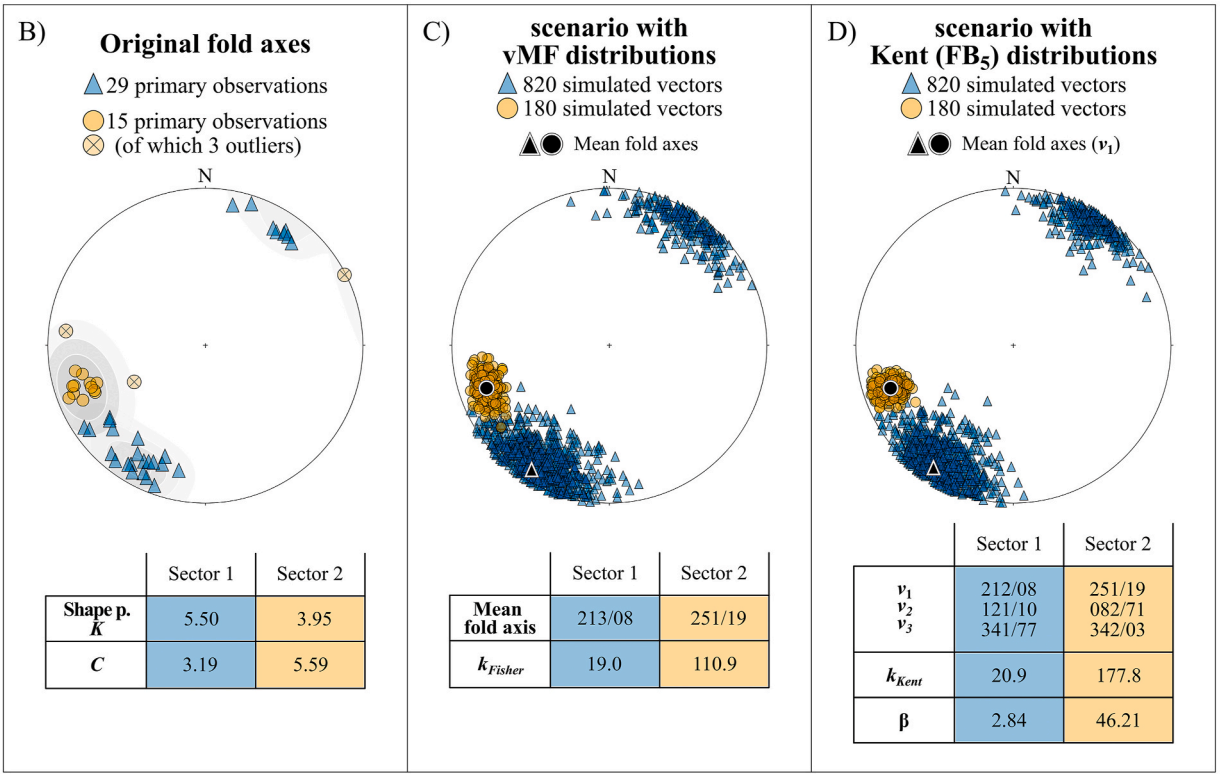

	Sector 1	Sector 2
Shape p. K	5.50	3.95
C	3.19	5.59

	Sector 1	Sector 2
Mean fold axis	213/08	251/19
k_{Fisher}	19.0	110.9

	Sector 1	Sector 2
v_1 v_2 v_3	212/08 121/10 341/77	251/19 082/71 342/03
k_{Kent}	20.9	177.8
β	2.84	46.21

(caption on next page)

Fig. 8. Choice of simulation parameters for stochastic simulation of fold axes. Methodology detailed in Sect. 4.2. A) Structural map, with colours, names, and acronyms as in Fig. 1. Black rectangle bounds the analysed area. Location of direct observations of fold axes in map view. Black and white dashed line separates the two structurally distinct sectors. B) Stereogram of original fold axes with results of eigen analysis (K and C parameters for Sectors 1 and 2). C) Stereogram of N_v = 1000 simulated fold axes, mirroring the von Mises-Fisher distribution parameterised from data in (B). vMF parameters in table. D) Stereogram of N_v = 1000 simulated fold axes, mirroring the Kent distribution parameterised from data in (B). Kent parameters in the table. In (B), (C) and (D), Sector 1 is represented by blue triangles, Sector 2 by light orange circles. Mean fold axes as black symbols. (For interpretation of the references to colour in this figure legend, the reader is referred to the Web version of this article.)

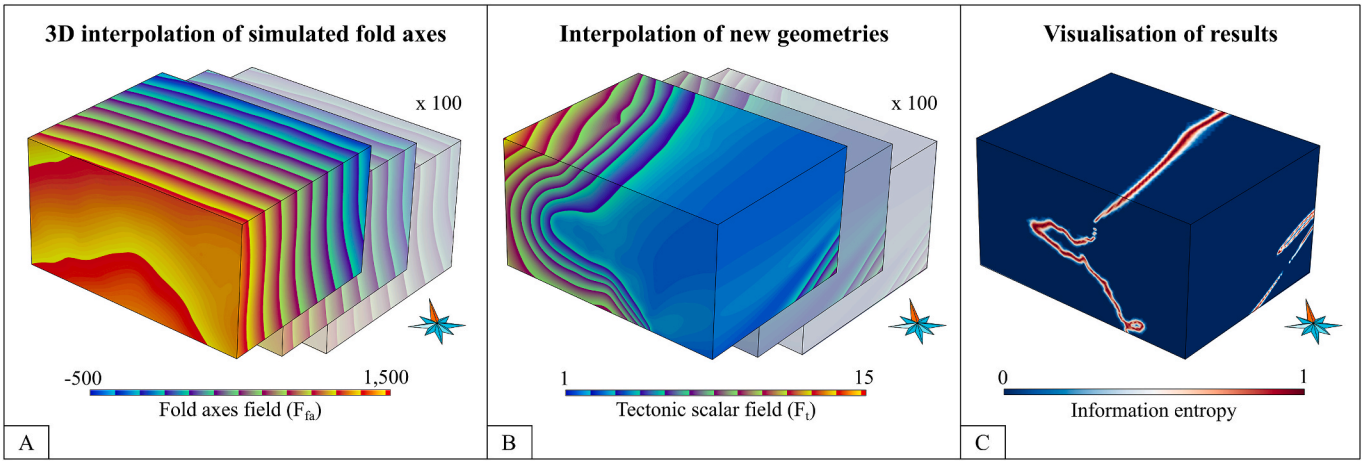

Fig. 9. Uncertainty workflow, as detailed in Sect. 3.6 (workflow) and 4.2 (application). Location of the investigated volume is indicated in Fig. 1A by the dashed rectangle. A) Interpolation of N_r = 100 fold axes fields from original and simulated fold axes (considering a single statistical scenario). B) Interpolation of N_r = 100 new geometries. C) Visualisation of results with information entropy (Wellmann and Regenauer-Lieb, 2012).

approximately 100 m and a horizontal shift of about 70 m. The results also indicate that the minor southeastern isoclinal fold tends to close along the axial plane (Fig. 11 B–B' section). Moreover, portions of the folds also undergo counterclockwise and clockwise rotations, ultimately adopting inclined NW-dipping and SE-dipping geometries (Fig. 11 B–B' section), for which we do not provide a detailed explanation that is beyond the scope of this contribution. The series of parallel cross-sections also underlines the non-cylindrical nature of the fold since, moving from section E-E′ to section B-B' (Figs. 10 and 11), it is evident how the fold hinges get closer due to converging mean fold axes.

As highlighted in Fig. 11, the assumption of vMF against Kent distributions generates different models but similar fold geometries. While the general behaviours just described such as the partial rotation of sectors of the folds and possible closure along the axial plane are common, the comparison between entropies indicate shifts in the location of portion of the folds (in the order of ca. 100 m), caused by the different ovalness parameters of the distributions ($\beta = 0$ for vMF and $\beta \neq 0$ for Kent). In section B-B' (Fig. 11), higher entropy values for the vMF scenario are concentrated at shallower depths for the limbs of the northwestern portion of the fold, behaviour that instead results reversed for the southeastern smaller fold. As expected, higher differences in entropies between scenarios are registered away from constraining data.

Finally, since interpolating or extrapolating in the subsurface or the eroded part of the simulated volume is equivalent from a mathematical perspective (though yielding different practical applications), we present the solution of the uncertainty analysis in both domains (see Figs. 10 and 11).

5. Discussion

We have applied the implicit modelling approach for the representation of a 9 km^2 portion of the Pennine Italian Alps situated on the right bank of the Valtournenche valley, around the Cignana Lake area. This area is within the scope of a previously developed regional 3D structural model presented by Arienti et al. (2024) which covers the entire transect from Mont Blanc to Monte Rosa. In the larger regional model, the geometry of tectonic boundaries relied heavily on structural interpretations drawn on vertical cross-sections that played a crucial role in propagating structural and geological information from the outcrop scale to the regional scale. In contrast, given the smaller size of the Cignana Lake area and the wealth of structural measurements, the methodology proposed in this work avoids using interpretations on vertical cross-sections, thus reducing the subjective contribution of the interpreter. With respect to the regional-scale model by Arienti et al. (2024), we have also improved the resolution of the model and now the reconstruction better adheres to geological and structural data collected at outcrops.

For the modelling of folds, we employ a strategy based on the work of Laurent et al. (2016) and perform 3D interpolation of fold axes' vectors to homogenise structural control on the interpolation. Differently from previous works (Laurent et al., 2016; Grose et al., 2017, 2018, 2021), our work does not introduce constraints about the axial surfaces and instead leverages the rich database of fold axes measurements. This is partly due to the difficulties in tracing the univocal envelopment of hinge lines (i.e., the axial surface) in our complex metamorphic setting. In fact, in our study area the folded schistosity is the result of multiple tectonic events that have transposed and obliterated the original geological contacts, and folds develop across various scales drawing parasitic geometries. Moreover, the absence of clear indicators of the stratigraphic polarity often makes it difficult to distinguish separate fold limbs when these are sub-parallel, such as for the isoclinal folds that we model.

This modelling approach of interpolation of fold axes, in addition to the densification of position constraints through projection of the mapped tectonic contacts in the fold axes directions presented in Sect. 3.5, enabled the representation of non-cylindrical geometries that preserve model-resolution variability of fold axes. Due to the nature of disharmonic fold geometries, whose behaviour is strongly influenced by the rheologic characteristics of the rocks they deform, predicting geometries that cannot be observed at surface is difficult. Therefore, no assumption of harmonic behaviour was made in this study and, instead, our geomodelling workflow aims at leveraging the surface database and

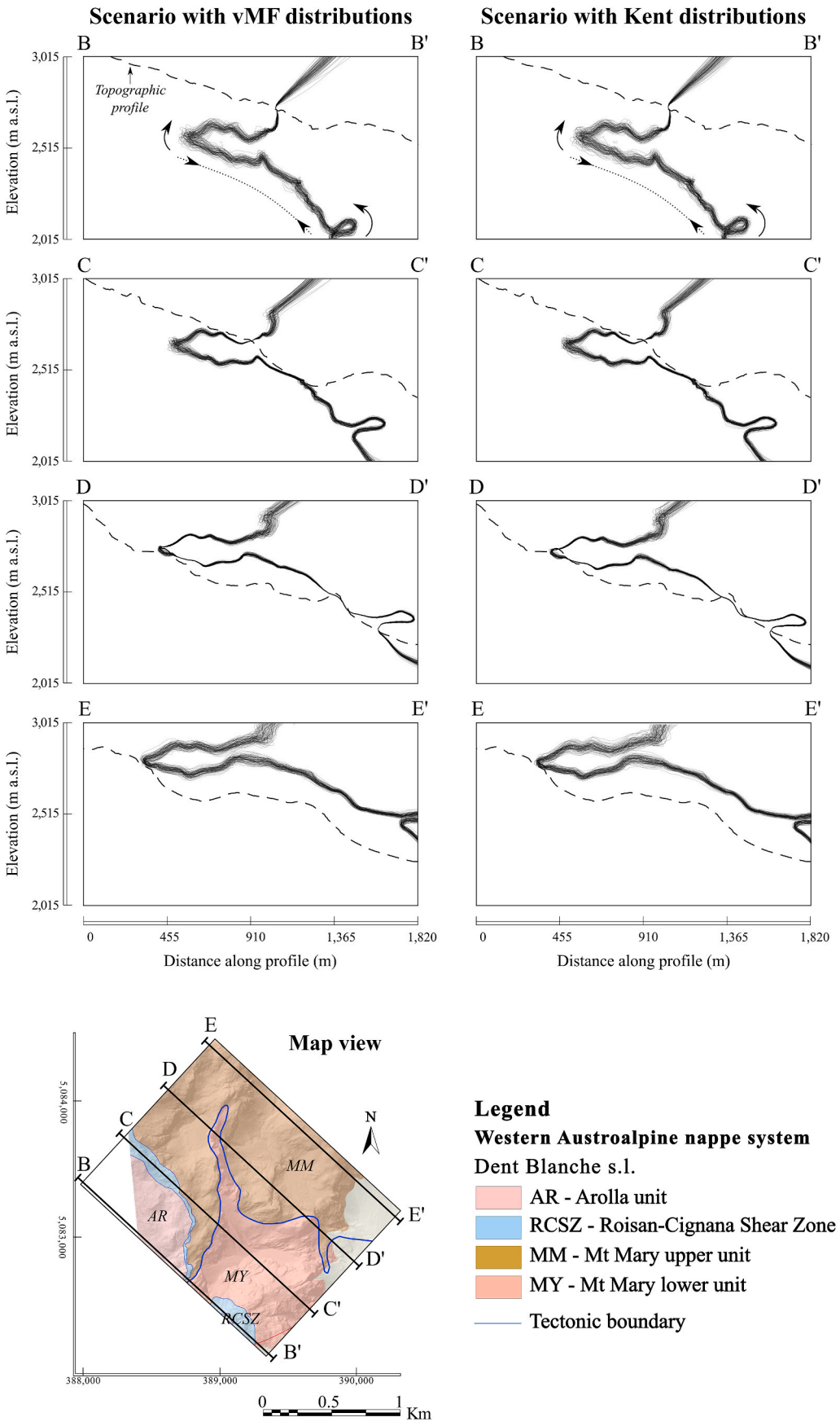

Fig. 10. Result of the 200 realisations displayed on vertical cross-sections ($N_r = 100$ for the scenario with vMF distribution on the left, and $N_r = 100$ for Kent distribution on the right). Intersection lines between the generated geometries and the cross-sections planes. The area of investigation is shown in map view at the bottom of the figure (location is indicated in Fig. 1A by the dashed rectangle). Description of the results in Sect. 4.2.

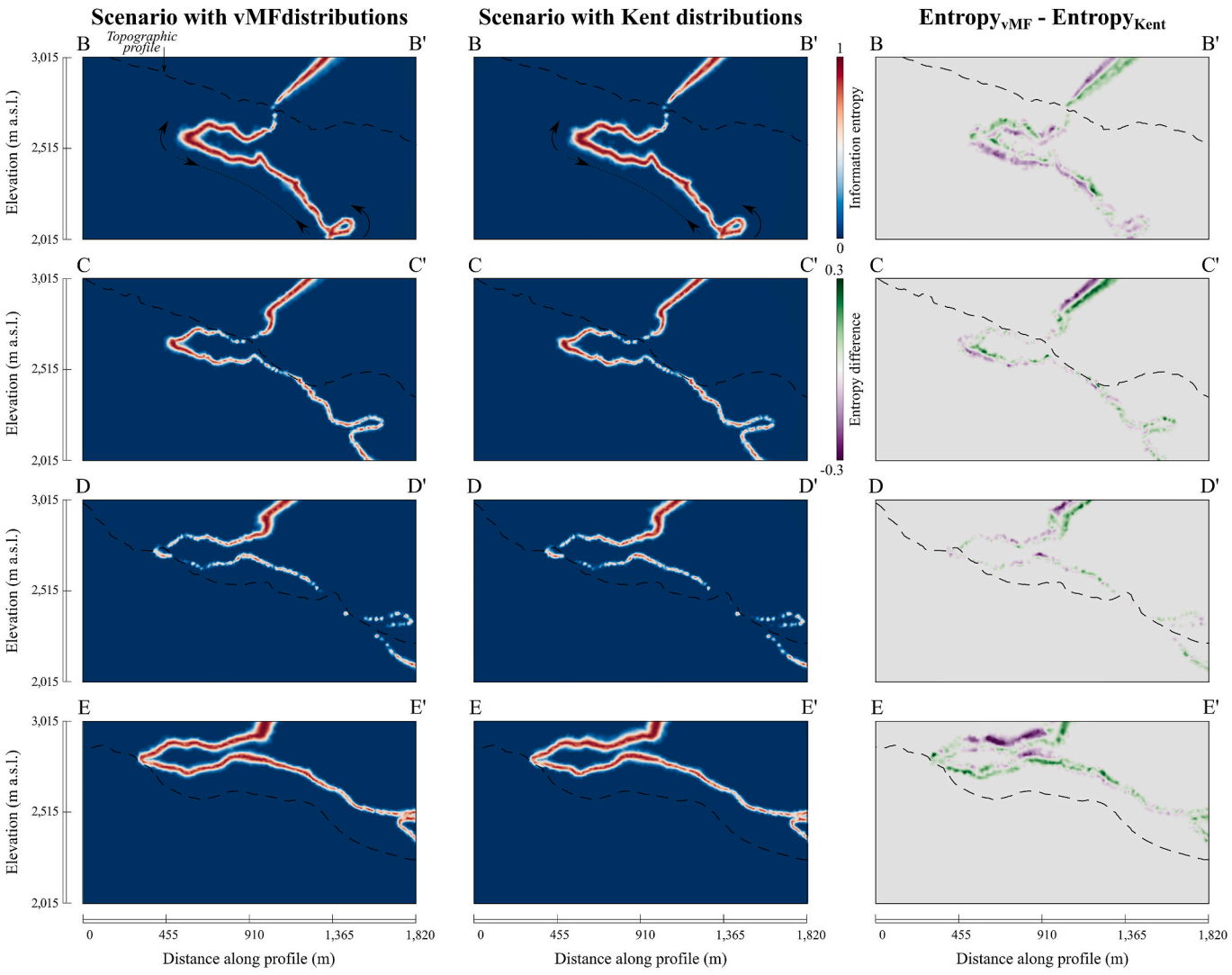

Fig. 11. Result of the 200 realisations displayed on vertical cross-sections ($N_r = 100$ for the scenario with vMF distribution on the left, and $N_r = 100$ for Kent distribution in the middle column): information entropy at cross-section's locations. On the right, difference between entropies. The area of investigation is shown in map view at the bottom of Fig. 10. Description of the results in Sect. 4.2.

its components, including the rugged topography that allows the three-dimensionality of the dataset. This is advantageous in regions where fold wavelengths may vary in space but calls for well sampled study areas, as hinges in the model are only supported by sample data. In areas where unseen fold hinges are suspected, it is advised either to generate virtual stratigraphic samples as proposed in this work for fold axis, or to rely on the periodic model of Grose et al. (2017).

A limitation to the faithful representation of disharmonic, similar, and particularly isoclinal folds, arises from the difficulty of the DSI implicit interpolator to enable thickness variations, that implies strong variations in the modulus of the gradient of the potential field in the implicit approach. This is primarily due to the imposition of the constant gradient constraint (Frank et al., 2007) in the interpolation and to the use of linear tetrahedra (Laurent, 2016). While this constraint is essential for ensuring the well-posedness of the mathematical problem and minimising gradient variations between adjacent tetrahedra, it is most suitable to model parallel fold and/or sedimentary sequences with almost constant thicknesses of layers (Laurent, 2016). In contrast, when applied to disharmonic, similar, and particularly isoclinal folds like in this study, the constant gradient constraint leads to a strong smoothing and to a "rebounding" effect away from observed features at depth, to maintain constant thicknesses within the layers. In this study we minimised, as much as possible, this effect by setting lower weights in the constant gradient compared to position and orientation constraints (as low as 10^{-5}). However, to further enhance the accuracy of the interpretation, future improvements may consider introducing explicit anisotropies in the regularisation term of the scalar field that models the tectonic contacts (Laurent et al., 2016; Pizzella et al., 2022; Belhachmi et al., 2024), to better capture the intricacies of geological structures characterised by non-uniform lateral homogeneous thicknesses and enhancing the geological realism.

Our workflow proposes, in addition to the generation of a deterministic 3D structural model for the whole Cignana area, the incorporation of uncertainties affecting the database of fold axes measurements and the analysis of their effects on isoclinal recumbent folds exposed in the area. Since the strategies implemented in our workflow for the modelling of folds are primarily affected by fold axes vectors, our uncertainty analysis focused on the simulation of alternative suites of fold axes according to orientation distributions derived from the input database, in a workflow inspired to the work of Lindsay et al. (2012). We use simulated fold axes alongside our original field observations to deal with the challenge of limited and sparse data sampling. These simulated axes act as extra measurements we would expect to gather if we were able to do more sampling, like drilling boreholes or conducting more

fieldwork.

The sources of uncertainty affecting our uncertainty analysis are multiple and not easily distinguishable. Given that we rely on manually collected field data for the statistical characterisation of spherical distributions and subsequent generation of fold axes, the entropy resulting from the multiple realisations is also intrinsically affected by the instrumental uncertainty of these measurements.

By employing stochastic algorithms to generate both trend/plunge values and (x, y, z) locations of the simulated fold axes, our objective is to reproduce a double randomness inherent in field data. On one hand, we represent the dispersion in orientation of the planar and linear elements of a metamorphic fabric (foliations and lineations), which can be parameterised with spherical statistical models such as vMF or Kent distributions. On the other hand, we aim at reproducing the apparent randomness that characterises the spatial distribution of structural measurements collected in the field, which often exhibit densely populated clusters juxtaposed with areas with more sparsely distributed measurements. This spatial variability is influenced by factors such as outcrop availability and accessibility, which in turn are affected by a multitude of variables among which geomorphological processes, collectively dictating the paths taken by field structural geologists. Alternatively, other sampling methodologies for positioning the simulated fold axes could envision enforcing minimum distances among the N_v simulated vectors, granting the workflow better control over spatial correlations, which are instead primarily influenced by the density of the simulated sample in our study. This approach could also allow drawing parallels with techniques such as the pilot points method (e.g., Certes and de Marsily, 1991), mainly utilised in hydrogeology and geophysics.

6. Conclusions

We have built three-dimensional structural models of the Lago di Cignana area by relying on high-resolution geological mapping and an extensive dataset of schistosity and fold axis structural measurements. Within this model, we have represented the tectonic boundaries exposed in the area, some of which are major Alpine shear structures such as the Roisan-Cignana Shear Zone, the Dent Blanche Basal Thrust and the Combin Fault. Our interpolation workflow employs the Discrete Smooth Interpolator algorithm, allowing to impose the tectonic surfaces to align with the foliation planes and fold axes vectors. For the modelling of open and isoclinal folds, we have incorporated the 3D implicit interpolation of fold axes and imposed the interpolated directions as tangent constraints on the interpolation of the fold geometries. Furthermore, we have integrated stochastic simulations of fold axes following von Mises-Fisher and Kent models, and quantitatively assessed the uncertainty of isoclinal recumbent folds with this method. This yielded important insights into the position of fold hinge sectors and the potential rotation of the axial plane, which are of great importance when modelling three-dimensional structures, since fold hinges are often complex structures and can serve as focal regions for subsurface fluid or gas migration. They may also be sites where localised crenulation cleavage develops and might impact stress distribution and mechanical behaviour in rock masses. The outcoming 200 realisations display partial rotation of the axial plane, closure along the fold axis direction of the isoclinal fold, and higher uncertainty values at fold hinges.

CRediT authorship contribution statement

Gloria Arienti: Writing – original draft & review & editing, Conceptualisation, Methodology, Field Data Collection, Data curation, Structural analysis, Software, Visualisation. Andrea Bistacchi: Writing – review & editing, Conceptualisation, Field Data Collection, Funding acquisition. Guillaume Caumon: Writing – review & editing, Methodology, Software, Conceptualisation. Bruno Monopoli: Writing – review & editing, Field Data Collection, Data curation. Giovanni Dal Piaz: Field Data Collection, Data curation.

Declaration of competing interest

The authors declare that they have no conflict of interest.

Acknowledgements

AspenTech is acknowledged for licenses of the SKUA/GOCAD software. Our study was supported by the Interreg European RESERVAQUA project (ID 551749). G. Arienti acknowledges support from the European Union's Erasmus Traineeship + program, and G. Caumon thanks the RING Consortium (www.ring-team.org/Consortium) for supporting the development of RINGToolkit. We warmly thank Z. Lugoboni for helping with data collection and G.V. Dal Piaz for introducing all of us to this area, where he carried out an invaluable work in almost 70 years of fieldwork and detailed structural, petrographic and geochronological analysis. Finally, we thank the editor F. Agosta, an anonymous reviewer, and E. Fazio for their insightful comments.

Data availability

Data will be made available on request.

References

Allmendinger, R.W., Cardozo, N., Fisher, D.M., 2015. Structural Geology Algorithms: Vectors and Tensors. Cambridge University Press, Cambridge.

Argand, E., 1911. Les nappes de recouvrement des Alpes pennines et leurs prolongements structuraux. Mater. Carte Geol. Suisse 31, 1–26.

Argand, E., 1906. Sur la tectonique du Massif de la Dent Blanche. Comptes Rendus de l'Académie Des Sciences, Paris.

Argand, E., 1909. L'exploration géologique des Alpes pennines centrales. Bulletin de La Société Vaudoise Des Sciences Naturelles 45, 217–276.

Arienti, G., Bistacchi, A., Caumon, G., Dal Piaz, G., Monopoli, B., Bertolo, D., 2024. Regional-scale 3D modelling in metamorphic belts: an implicit model-driven workflow applied in the Pennine Alps. J. Struct. Geol. 180, 105045. https://doi.org/10.1016/j.jsg.2023.105045.

Ballèvre, M., Merle, O., 1993. The Combin Fault : compressional reactivation of a late cretaceous-early tertiary detachment fault in the western Alps. Schweizerische Mineralogische Und Petrographische Mitteilungen 73, 205–227.

Belhachmi, A., Benabbou, A., Mourrain, B., 2024. A spline-based regularized method for the reconstruction of complex geological models. Math. Geosci. https://doi.org/10.1007/s11004-024-10149-2.

Bistacchi, A., Dal Piaz, G., Massironi, M., Zattin, M., Balestrieri, M., 2001. The aosta–ranzola extensional fault system and oligocene–present evolution of the austroalpine–penninic wedge in the northwestern. https://doi.org/10.1007/s005310000178.

Bistacchi, A., Massironi, M., 2000. Post-nappe brittle tectonics and kinematic evolution of the north-western Alps: an integrated approach. Tectonophysics 327, 267–292. https://doi.org/10.1016/S0040-1951(00)00206-7.

Bistacchi, A., Massironi, M., Dal Piaz, G.V, Dal Piaz, G., Monopoli, B., Schiavo, A., Toffolon, G., 2008. 3D fold and fault reconstruction with an uncertainty model: an example from an Alpine tunnel case study. Comput. Geosci. 34, 351–372. https://doi.org/10.1016/j.cageo.2007.04.002.

Bond, C.E., 2015. Uncertainty in structural interpretation: lessons to be learnt. J. Struct. Geol. 74, 185–200. https://doi.org/10.1016/j.jsg.2015.03.003.

Borradaile, G., 2003. Statistics of Earth Science Data. Springer Berlin Heidelberg, Berlin, Heidelberg. https://doi.org/10.1007/978-3-662-05223-5.

Bucher, K., 2005. Blueschists, eclogites, and decompression assemblages of the Zermatt-Saas ophiolite: high-pressure metamorphism of subducted Tethys lithosphere. Am. Mineral. 90, 821–835. https://doi.org/10.2138/am.2005.1718.

Caby, R., 1981. Le Mésozoïque de la zone du Combin en Val d'Aoste (Alpes Graies): Imbrications tectoniques entre séries issues des domaines pennique, austroalpin et océanique. Geol. Alpine 57, 5–13.

Calcagno, P., Chilès, J.P., Courrioux, G., Guillen, A., 2008. Geological modelling from field data and geological knowledge. Part I. Modelling method coupling 3D potential-field interpolation and geological rules. Phys. Earth Planet. In. 171, 147–157. https://doi.org/10.1016/j.pepi.2008.06.013.

Cardozo, N., Allmendinger, R.W., 2013. Spherical projections with OSXStereonet. Comput. Geosci. 51, 193–205. https://doi.org/10.1016/j.cageo.2012.07.021.

Caumon, G., Gray, G., Antoine, C., Titeux, M.O., 2013. Three-dimensional implicit stratigraphic model building from remote sensing data on tetrahedral meshes: Theory and application to a regional model of la Popa Basin, NE Mexico. IEEE Trans. Geosci. Rem. Sens. 51, 1613–1621. https://doi.org/10.1109/TGRS.2012.2207727.

Caumon, G., L Tertois, A., Zhang, L., 2007. Elements for stochastic structural perturbation of stratigraphic models. In: EAGE Conference on Petroleum

Geostatistics. European Association of Geoscientists & Engineers. https://doi.org/10.3997/2214-4609.201403041.
Certes, C., de Marsily, G., 1991. Application of the pilot point method to the identification of aquifer transmissivities. Adv. Water Resour. 14, 284–300. https://doi.org/10.1016/0309-1708(91)90040-U.
Cherpeau, N., Caumon, G., 2015. Stochastic structural modelling in sparse data situations. Petrol. Geosci. 21, 233–247. https://doi.org/10.1144/petgeo2013-030.
Chilès, J.P., Aug, C., Guillen, A., Lees, T., 2004. Modelling the geometry of geological units and its uncertainty in 3D from structural data: the potential-field method. In: Proceedings of International Symposium on Orebody Modelling and Strategic Mine Planning. Perth, pp. 313–320.
Compagnoni, R., Dal Piaz, G.V., Hunziker, J.C., Gosso, G., Lombardo, B., Williamns, P.F., 1977. The Sesia-Lanzo zone, a slice of continental crust with Alpine high pressure-low temperature assem-blages in the Western Italian Alps. Rendiconti della Soc. Ital. Mineral. Petrol. 33, 281–334.
Coward, M., Dietrich, D., 1989. Alpine Tectonics — an Overview, vol. 45. Geological Society, London, Special Publications, pp. 1–29. https://doi.org/10.1144/GSL.SP.1989.045.01.01.
Dal Piaz, G.V., Bistacchi, A., Gianotti, F., Monopoli, B., Passeri, L., Schiavo, A., Bertolo, D., Bonetto, F., Ciarapica, G., Dal Piaz, G., Gouffon, Y., Massironi, M., Ratto, S., Toffolon, G., 2016. Foglio 070 Cervino e Note Illustrative. Carta Geologica d'Italia Alla Scala 1:50.000. ISPRA, Regione Autonoma Valle d'Aosta, p. 432.
Dal Piaz, G.V., Gianotti, F., Monopoli, B., Pennacchioni, G., Tartarotti, P., Schiavo, A., Carraro, F., Bistacchi, A., Massironi, M., Martin, S., Ratto, S., 2010. Foglio 091 Chatillon e Note Illustrative. Carta Geologica d'Italia Alla Scala 1:50.000. ISPRA, Regione Autonoma Valle d'Aosta, p. 152.
Dal Piaz, G.V., 2001. History of tectonic interpretations of the Alps. J. Geodyn. 32, 99–114. https://doi.org/10.1016/S0264-3707(01)00019-9.
Dal Piaz, G.V., 1999. The Austroalpine-Piedmont nappe stack and the puzzle of Alpine Tethys. Mem. Sci. Geol. 53, 153–162.
Dal Piaz, G.V., Bistacchi, A., Massironi, M., 2003. Geological outline of the Alps. Episodes Journal of International Geoscience 26, 175–180. https://doi.org/10.18814/EPIIUGS/2003/V26I3/004.
Dal Piaz, G.V., Ernst, W.G., 1978. Areal geology and petrology of eclogites and associated metabasites of the Piemonte ophiolite nappe, breuil—st. Jacques area, Italian Western Alps. Tectonophysics 51, 99–126. https://doi.org/10.1016/0040-1951(78)90053-7.
de Kemp, E.A., 2000. 3-D visualization of structural field data: examples from the Archean Caopatina Formation, Abitibi greenstone belt, Québec, Canada. Comput. Geosci. 26, 509–530. https://doi.org/10.1016/S0098-3004(99)00142-9.
de Kemp, E.A., Schetselaar, E.M., Hillier, M.J., Lydon, J.W., Ransom, P.W., 2016. Assessing the workflow for regional-scale 3D geologic modeling: an example from the Sullivan time horizon, Purcell Anticlinorium East Kootenay region, southeastern British Columbia. Interpretation 4 (1), SM33–SM50. https://doi.org/10.1190/INT-2015-0191.
De La Varga, M., Schaaf, A., Wellmann, F., 2019. GemPy 1.0: open-source stochastic geological modeling and inversion. Geosci. Model Dev. (GMD) 12, 1–32. https://doi.org/10.5194/gmd-12-1-2019.
Diehl, E.A., Masson, H., Stutz, A.H., 1952. Contributo alla conoscenza del ricoprimento Dent Blanche. Memorie Istituti Geologia Mineralogia Università Di Padova 17, 53.
Ernst, W.G., Dal Piaz, G.V., 1978. Mineral parageneses of eclogitic rocks and related mafic schists of the Piemonte ophiolite nappe, Breuil-St. Jacques area, Italian Western Alps. Am. Mineral. 63, 621–640.
Fisher, N.I., Lewis, T., Embleton, B.J.J., 1987. Statistical Analysis of Spherical Data. Cambridge University Press.
Fisher, N.I., Lewis, T., Willcox, M.E., 1981. Tests of discordancy for samples from Fisher's distribution on the sphere. Applied Statistics 30, 230. https://doi.org/10.2307/2346346.
Fisher, R.A., 1953. Dispersion on a sphere. Proc. Roy. Soc. Lond. 217, 295–305.
Forster, M., Lister, G., Compagnoni, R., Giles, D., Hills, Q., Betts, P., Beltrando, M., Tamagno, E., 2004. Mapping of oceanic crust with" HP" to" UHP" metamorphism: The Lago di Cignana Unit (Western Alps). In: Pasquarè, G., Venturini, C., Groppelli, G. (Eds.), Mapping Geology in Italy. APAT - Dip. Difesa del Suolo. Serv. Geol. d'Italia, Roma, pp. 279–286.
Frank, T., Tertois, A.L., Mallet, J.L., 2007. 3D-reconstruction of complex geological interfaces from irregularly distributed and noisy point data. Comput. Geosci. 33, 932–943. https://doi.org/10.1016/j.cageo.2006.11.014.
Frezzotti, M.L., Selverstone, J., Sharp, Z.D., Compagnoni, R., 2011. Carbonate dissolution during subduction revealed by diamond-bearing rocks from the Alps. Nat. Geosci. 4, 703–706. https://doi.org/10.1038/ngeo1246.
Frodeman, R., 1995. Geological reasoning: geology as an interpretive and historical science. Geol. Soc. Am. Bull. 107 (2), 960–968. https://doi.org/10.1130/0016-7606(1995)107<0960:GRGAAI>2.3.CO.
Groppo, C., Beltrando, M., Compagnoni, R., 2009. The P-T path of the ultra-high pressure Lago Di Cignana and adjoining high-pressure meta-ophiolitic units: insights into the evolution of the subducting Tethyan slab. J. Metamorph. Geol. 27, 207–231. https://doi.org/10.1111/j.1525-1314.2009.00814.x.
Grose, L., Ailleres, L., Laurent, G., Armit, R., Jessell, M., 2019. Inversion of geological knowledge for fold geometry. J. Struct. Geol. 119, 1–14. https://doi.org/10.1016/j.jsg.2018.11.010.
Grose, L., Ailleres, L., Laurent, G., Jessell, M., 2021. LoopStructural 1.0: time-aware geological modelling. Geosci. Model Dev. (GMD) 14, 3915–3937. https://doi.org/10.5194/gmd-14-3915-2021.
Grose, L., Laurent, G., Aillères, L., Armit, R., Jessell, M., Caumon, G., 2017. Structural data constraints for implicit modeling of folds. J. Struct. Geol. 104, 80–92. https://doi.org/10.1016/j.jsg.2017.09.013.
Grose, L., Laurent, G., Aillères, L., Armit, R., Jessell, M., Cousin-Dechenaud, T., 2018. Inversion of structural geology data for fold geometry. J. Geophys. Res. Solid Earth 123, 6318–6333. https://doi.org/10.1029/2017JB015177.
Hillier, M., de Kemp, E., Schetselaar, E., 2013. 3D form line construction by structural field interpolation (SFI) of geologic strike and dip observations. J. Struct. Geol. 51, 167–179. https://doi.org/10.1016/j.jsg.2013.01.012.
Hillier, M.J., Schetselaar, E.M., de Kemp, E.A., Perron, G., 2014. Three-dimensional modelling of geological surfaces using generalized interpolation with radial basis functions. Math. Geosci. 46, 931–953. https://doi.org/10.1007/s11004-014-9540-3.
Houlding, S.W., 1994. The Geological Characterization Process. 3D Geoscience Modeling. Springer Berlin Heidelberg, Berlin, Heidelberg, pp. 7–26. https://doi.org/10.1007/978-3-642-79012-6_2.
Irakarama, M., Thierry-Coudon, M., Zakari, M., Caumon, G., 2022. Finite element implicit 3D subsurface structural modeling. Comput. Aided Des. 149, 103267. https://doi.org/10.1016/j.cad.2022.103267.
Kaufmann, O., Martin, T., 2009. Reprint of "3D geological modelling from boreholes, cross-sections and geological maps, application over former natural gas storages in coal mines" [Comput. Geosci. 34 (2008) 278-290]. Comput. Geosci. 35, 70–82. https://doi.org/10.1016/S0098-3004(08)00227-6.
Kent, J.T., 1982. The Fisher-bingham distribution on the sphere. J. Roy. Stat. Soc. 44, 71–80.
Kirst, F., 2017. Polyphase greenschist-facies reactivation of the dent Blanche basal thrust (western Alps) during progressive alpine orogeny. Swiss J. Geosci. 110, 503–521. https://doi.org/10.1007/s00015-017-0264-5.
Kirst, F., Leiss, B., 2017. Kinematics of syn- and post-exhumational shear zones at Lago di Cignana (Western Alps, Italy): constraints on the exhumation of Zermatt–Saas (ultra) high-pressure rocks and deformation along the Combin Fault and Dent Blanche Basal Thrust. Int. J. Earth Sci. 106, 215–236. https://doi.org/10.1007/s00531-016-1316-1.
Lajaunie, C., Courrioux, G., Manuel, L., 1997. Foliation fields and 3D cartography in geology: principles of a method based on potential interpolation. Math. Geol. 29, 571–584. https://doi.org/10.1007/BF02775087.
Laurent, G., 2016. Iterative thickness regularization of stratigraphic layers in discrete implicit modeling. Math. Geosci. 48, 811–833. https://doi.org/10.1007/s11004-016-9637-y.
Laurent, G., Ailleres, L., Grose, L., Caumon, G., Jessell, M., Armit, R., 2016. Implicit modeling of folds and overprinting deformation. Earth Planet Sci. Lett. 456, 26–38. https://doi.org/10.1016/j.epsl.2016.09.040.
Lindsay, M.D., Aillères, L., Jessell, M.W., de Kemp, E.A., Betts, P.G., 2012. Locating and quantifying geological uncertainty in three-dimensional models: analysis of the Gippsland Basin, southeastern Australia. Tectonophysics 546–547, 10–27. https://doi.org/10.1016/j.tecto.2012.04.007.
Mallet, J.L., 2002. Geomodeling. Oxford University Press.
Manzotti, P., 2011. Petro-structural map of the dent Blanche tectonic system between valpelline and Valtournenche valleys, western Italian Alps. J. Maps 7, 340–352. https://doi.org/10.4113/jom.2011.1179.
Manzotti, P., Ballèvre, M., Pitra, P., Schiavi, F., 2021. Missing lawsonite and aragonite found: P–T and fluid composition in meta-marls from the Combin Zone (Western Alps). Contrib. Mineral. Petrol. 176, 60. https://doi.org/10.1007/s00410-021-01818-0.
Manzotti, P., Ballèvre, M., Zucali, M., Robyr, M., Engi, M., 2014a. The tectonometamorphic evolution of the Sesia-Dent Blanche nappes (internal Western Alps): review and synthesis. Swiss J. Geosci. 107, 309–336. https://doi.org/10.1007/s00015-014-0172-x.
Manzotti, P., Zucali, M., Ballèvre, M., Robyr, M., Engi, M., 2014b. Geometry and kinematics of the roisan-cignana shear zone, and the orogenic evolution of the dent Blanche tectonic system (western Alps). Swiss J. Geosci. 107, 23–47. https://doi.org/10.1007/s00015-014-0157-9.
Maxelon, M., Mancktelow, N.S., 2005. Three-dimensional geometry and tectonostratigraphy of the pennine zone, central Alps, Switzerland and northern Italy. Earth Sci. Rev. 71, 171–227. https://doi.org/10.1016/j.earscirev.2005.01.003.
Maxelon, M., Renard, P., Courrioux, G., Brändli, M., Mancktelow, N., 2009. A workflow to facilitate three-dimensional geometrical modelling of complex poly-deformed geological units. Comput. Geosci. 35, 644–658. https://doi.org/10.1016/j.cageo.2008.06.005.
Nabavi, S.T., Fossen, H., 2021. Fold geometry and folding – a review. Earth Sci. Rev. 222, 103812. https://doi.org/10.1016/j.earscirev.2021.103812.
Pakyuz-Charrier, E., Lindsay, M., Ogarko, V., Giraud, J., Jessell, M., 2018. Monte Carlo simulation for uncertainty estimation on structural data in implicit 3-D geological modeling, a guide for disturbance distribution selection and parameterization. Solid Earth 9, 385–402. https://doi.org/10.5194/se-9-385-2018.
Passeri, L., Ciarapica, G., Dal Piaz, G.V., 2018. The problematic origin of the pancherotcime bianche-bettaforca unit (PCB) in the piemonte zone (western Alps). Italian Journal of Geosciences 137, 478–489. https://doi.org/10.3301/IJG.2018.21.
Peacock, D.C.P., Nixon, C.W., Rotevatn, A., Sanderson, D.J., Zuluaga, L.F., 2017. Interacting faults. J. Struct. Geol. 97, 1–22. https://doi.org/10.1016/j.jsg.2017.02.008.
Perello, P., Gianotti, F., Monopoli, B., Carraro, F., Venturini, G., Fontan, D., Schiavo, A., Bonetto, F., 2011. Foglio 089 Courmayeur e Note Illustrative. Carta Geologica d'Italia Alla Scala 1:50.000. Regione Autonoma Valle d'Aosta, ISPRA, p. 152.
Philippon, M., de Veslud, C.L.C., Gueydan, F., Brun, J.P., Caumon, G., 2015. 3D geometrical modelling of post-foliation deformations in metamorphic terrains (Syros, Cyclades, Greece). J. Struct. Geol. 78, 134–148. https://doi.org/10.1016/j.jsg.2015.07.002.
Pizzella, L., Alais, R., Lopez, S., Freulon, X., Rivoirard, J., 2022. Taking better advantage of foldfold Axis data to characterize anisotropy of complex folded structures in the

implicit modeling framework. Math. Geosci. 54, 95–130. https://doi.org/10.1007/s11004-021-09950-0.
Pleuger, J., Roller, S., Walter, J.M., Jansen, E., Froitzheim, N., 2007. Structural evolution of the contact between two Penninic nappes (Zermatt-Saas zone and Combin zone, Western Alps) and implications for the exhumation mechanism and palaeogeography. Int. J. Earth Sci. 96, 229–252. https://doi.org/10.1007/s00531-006-0106-6.
Polino, R., Malusà, M.G., S, M., Carraro, F., Gianotti, F., Bonetto, F., Perello, P., Schiavo, A., Gouffon, Y., 2015. Foglio 090 Aosta e Note Illustrative. Carta Geologica d'Italia Alla Scala 1:50.000. Regione Autonoma Valle d'Aosta, ISPRA, p. 144.
Ramsay, J.G., 1967. Folding and Fracturing of Rocks. McGraw-Hill, New York.
Reddy, S.M., Wheeler, J., Butler, R.W.H., Cliff, R.A., Freeman, S., Inger, S., Pickles, C., Kelley, S.P., 2003. Kinematic reworking and exhumation within the convergent Alpine Orogen. Tectonophysics 365, 77–102. https://doi.org/10.1016/S0040-1951(03)00017-9.
Reinecke, T., 1998. Prograde high- to ultrahigh-pressure metamorphism and exhumation of oceanic sediments at Lago di Cignana, Zermatt-Saas Zone, western Alps. Lithos 42, 147–189. https://doi.org/10.1016/S0024-4937(97)00041-8.
Schneeberger, R., de La Varga, M., Egli, D., Berger, A., Kober, F., Wellmann, F., Herwegh, M., 2017. Methods and uncertainty estimations of 3-D structural modelling in crystalline rocks: a case study. Solid Earth 8, 987–1002. https://doi.org/10.5194/se-8-987-2017.
Shannon, E.C., 1948. A mathematical theory of communication. Bell System Technical Journal 27, 379–423.
Steck, A., Bigioggero, B., Dal Piaz, G.V., Escher, A., Martinotti, G., Masson, H., 1999. Carta tectonique des Alpes de Suisse occidentale et des régions avoisinantes. Service Hydrologique et Géologique National Carte spéc, 4 feuilles, 1:100.000.
Stockwell, C.H., 1950. The use of plunge in the construction of cross-sections of folds. Proceedings of the Geological Society of Canada 3, 97–121.
Sue, C., Delacou, B., Champagnac, J.D., Allanic, C., Tricart, P., Burkhard, M., 2007. Extensional neotectonics around the bend of the Western/Central Alps: an overview. Int. J. Earth Sci. 96, 1101–1129. https://doi.org/10.1007/S00531-007-0181-3.
Thornton, J.M., Mariethoz, G., Brunner, P., 2018. A 3D geological model of a structurally complex alpine region as a basis for interdisciplinary research. Sci. Data 5, 180238. https://doi.org/10.1038/sdata.2018.238.
Vollgger, S.A., Cruden, A.R., Ailleres, L., Cowan, E.J., 2015. Regional dome evolution and its control on ore-grade distribution: insights from 3D implicit modelling of the Navachab gold deposit, Namibia. Ore Geol. Rev. 69, 268–284. https://doi.org/10.1016/j.oregeorev.2015.02.020.
Wellmann, F., Caumon, G., 2018. 3-D Structural geological models: concepts, methods, and uncertainties. Adv. Geophys. 59, 1–121. https://doi.org/10.1016/bs.agph.2018.09.001.
Wellmann, J.F., Horowitz, F.G., Schill, E., Regenauer-Lieb, K., 2010. Towards incorporating uncertainty of structural data in 3D geological inversion. Tectonophysics 490, 141–151. https://doi.org/10.1016/j.tecto.2010.04.022.
Wellmann, J.F., Regenauer-Lieb, K., 2012. Uncertainties have a meaning: information entropy as a quality measure for 3-D geological models. Tectonophysics 526–529, 207–216. https://doi.org/10.1016/j.tecto.2011.05.001.
Wood, A.T., 1994. Simulation of the von mises fisher distribution. Commun. Stat. Simulat. Comput. 23, 157–164. https://doi.org/10.1080/03610919408813161.
Woodcock, N.H., 1977. Specification of fabric shapes using an eigenvalue method. Geol. Soc. Am. Bull. 88, 1231. https://doi.org/10.1130/0016-7606(1977)88<1231:SOFSUA>2.0.CO;2.
Wust, G.H., Silverberg, D.S., 1989. Northern Combin zone complex-Dent Blanche nappe contact: extension within the convergent Alpine belt. Schweizerische Mineralogische Und Petrographische Mitteilungen 69, 251–259.
Yuan, T., 2021. The 8-parameter Fisher–Bingham distribution on the sphere. Comput. Stat. 36, 409–420. https://doi.org/10.1007/s00180-020-01023-w.